CORRECTING CONTROL PULSE DISTORTIONS IN SUPERCONDUCTING QUBITS

MASTER'S THESIS

Written by *Anna Torp Åkesson*
January 17, 2022

Supervised by
Morten Kjærgaard

UNIVERSITY OF COPENHAGEN

FACULTY: Faculty of Science

INSTITUTE: Niels Bohr Institute

AUTHOR(S):   Anna Torp Åkesson

EMAIL: cpv752@alumni.ku.dk

TITLE AND SUBTITLE: Correcting Control Pulse Distortions in Superconducting Qubits
-

SUPERVISOR(S):   Morten Kjærgaard

HANDED IN: January 17, 2022

DEFENDED: February 8, 2022

NAME _____

SIGNATURE _____

DATE _____

Abstract

Pulses used for implementation of qubit gates are often subject to distortions arising from electrical components on the control line. These distortions negatively affect the gate performance and must be corrected in order to perform the wanted operations and have control of the qubit. This thesis focuses on distortions of flux pulses used for implementing two-qubit gates in flux-tunable transmons. The project consists of two parts: characterization and correction of signal distortions in four bias tees in a room-temperature setup, and a simulated experiment using the distorted waveforms. This simulation is based on the cryoscope method introduced in Rol et al.[1] where the flux pulse distortions are studied by reconstructing the pulse shape from its effect on the qubit. While correction of the bias tee distortions using the underlying physical parameters is not fully achieved, another approach is attempted, effectively correcting the pulse distortions without physically realistic parameters. The cryoscope simulation shows that reconstruction of pulses is possible, even for a simpler approach than originally proposed.

Contents

1 Introduction

Quantum computing utilizes the features of quantum systems in order to speed up classical algorithms. Classical computers have shortcomings when it comes to simulating quantum systems, since they run out of storage to represent quantum mechanical systems [2]. Furthermore, certain algorithms have not yet been possible to run on a classical computer due to the scaling of the complexity of them. Due to quantum parallelism and quantum interterference[3], quantum computers are capable of solving much more complex problems than a classical computer, and since they are themselves quantum systems, quantum simulations are made possible.
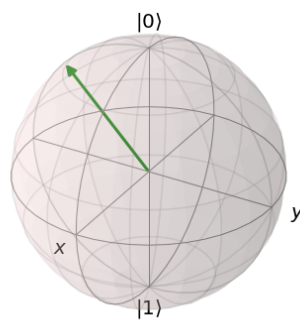

Figure 1: The Bloch sphere, a visualization tool for two level systems. Any qubit state can be represented on the sphere, like here for example the state $|\psi\rangle = \cos(\pi/8)|0\rangle + e^{i3\pi/2}\sin(\pi/8)|1\rangle$.

In order to physically implement quantum computing, one has to build a system that can be used as quantum bits, or qubits. These qubits can be realized physically in several different ways, but it is generally a challenging task because of the sensitivity to interactions with the environment, which shortens the lifetime of the qubit. However, regardless of how a quantum computer is realized, there are five requirements that must be fulfilled, known as the Divincenzio criteria [7][4]:

- The quantum system must be well-characterized, and scalable such that quantum computing can be realized for several qubits.

- One must be able to initialize the qubit in a reliable state such as the ground state.

- The qubit coherence times must be long enough to physically implement gates

- A set of quantum gates that implement any operation on the qubit is needed. This is referred to as a universal set of gates.

1

- Lastly, one must be able to measure the state of the qubit in order to extract the result of a given operation.

A way to describe and visualize qubit states is to represent them as vectors on the Bloch sphere, which is a tool for representing two-level system states on a unit sphere. Any state of the qubit can be visualized on the Bloch sphere as a vector originating in the center of the sphere. The $|0\rangle$ and $|1\rangle$ states are represented at north and south pole of the sphere, respectively, and the axis defined by these two states is referred to as the z-axis, also called the longitudinal axis. The transverse axes x and y span the equal superposition states $|\pm\rangle = \frac{1}{\sqrt{2}}(|0\rangle \pm |1\rangle)$ and $|\pm i\rangle = \frac{1}{\sqrt{2}}(|0\rangle \pm i|1\rangle)$. In polar coordinates, a pure qubit state $\cos(\theta)|0\rangle + e^{i\phi}\sin(\theta)|1\rangle$ can be represented as a Bloch vector of length 1 and, polar angle θ ($0 \leq \theta \leq \pi$) and azimuthal angle ϕ ($0 \leq \phi \leq 2\pi$). For a qubit with transition frequency $\omega_{01} > 0$ and Hamiltonian $H = \hbar\omega_{01}\sigma_z$, the unitary evolution describes the qubit as precessing around the z-axis. In a frame rotating with frequency ω_{01}, the Bloch vector is stationary on the Bloch sphere.

1.1 Superconducting qubits

There are several types of ways to realize qubits, for example via trapped ions, photons and spin qubits. These are "natural qubits", that is, parameters such as the transition energies are set by nature and cannot be modified. Another way to realize qubits is via engineered qubits, where the parameters describing the qubit can be engineered and optimized, giving more control of the system [5]. Superconducting qubits constitute an example of these engineered qubits and are made up of electrical circuits consisting of superconductors and other electrical elements. Several types of superconducting qubits exist, divided into groups of charge qubits, flux qubits and phase qubits. The focus in this thesis is on the transmon which is a special case of a charge qubit, but is also referred to as a charge/flux hybrid qubit.[**?**]

1.1.1 Superconductivity

Superconductivity is a phenomenon that occurs in certain materials where, if the material is cooled far below a critical temperature T_c, the resistance of the material decreases and becomes zero, and thus it behaves as a perfect conductor. This means that superconducting materials can be used in electronic circuits with no energy dissipation, and the low operating temperatures are ideal for making qubits out of them, since long qubit coherence times require minimal thermal noise. Above the critical temperature, the superconductor acts as a normal conductor with resistance, but as it is cooled below the critical temperature, it starts to be partially superconducting, and the effect

gets more pronounced at even lower temperatures. What happens when $T < T_c$ is that the electrons in the superconductor form into the so-called superconducting condensate. At $T > T_c$, the electrons behave normally as fermions, and therefore they must fulfil the Pauli principle, namely that they must occupy different states. Below the critical temperature, electrons with opposite spins start forming pairs known as Cooper pairs, resulting in boson-like "particles" with spin 0. The pairs are formed by two electrons with opposite spin exchanging phonons (quanta of vibrational energy) that exist in the lattice structure that make up the material. In normal conductors, phonons, along with imperfect lattice structure, are what causes resistance. If one of the electrons of a Cooper pair scatters from an irregularity in the lattice structure, the phonon that is emitted is immediately absorbed by the other electron in the pair, resulting in conservation of the total momentum of the system. The wave function of each of the Coopers pair in the condensate is of the form:

$$\Phi(\mathbf{r}_1, \mathbf{r}_2) = \sum_j a_j \phi(\mathbf{r}_1, \mathbf{P}_j, \uparrow) \phi(\mathbf{r}_2, -\mathbf{P}_j, \downarrow), \tag{1}$$

where $\phi(\mathbf{r}, \mathbf{P}_j, \uparrow)$ is the wave function of one of the single electrons in the Cooper pair (here with spin up), and as seen from these single electron wavefunctions, the electrons have opposite momentum and spin, as required to form a Cooper pair. $|\Phi(\mathbf{r}_1\mathbf{r}_2)|^2$ is then the probability density of finding the electrons at positions $\mathbf{r}_1$ and $\mathbf{r}_2$. The symmetry of scattering events ensures that energy is conserved, and thereby that the pairs shift from different terms in the total wave function, meaning that the pairs cannot be excited unless the absorbed energy is enough to break up the Cooper pair, resulting in normal conductivity of individual electrons. This energy required to go from superconductivity to regular conductivity processes is referred to as Δ and is called the superconducting gap, referring to the fact that there is an energy gap in which there are no states available. This energy gap is an advantage for combatting thermal noise, since the gap is large enough that thermal noise cannot break up the Cooper pairs and result in energy dissipation from resistive current.

The Cooper pair wavefunction in equation 1 describes a Cooper pair "at rest", that is, no current is running through the superconductor, since the total momentum is zero. If current is flowing through a superconductor such that each Cooper pair now has total momentum $\mathbf{P}$, the single Cooper pair wavefunction is modified such that the single electron wavefunctions in each term now have additional momentum $\mathbf{P}/2$ [5]:

$$\Phi(\mathbf{r}_1, \mathbf{r}_2) = \sum_j a_j \phi(\mathbf{r}_1, \mathbf{P}_j + \mathbf{P}/2, \uparrow) \phi(\mathbf{r}_2, -\mathbf{P}_j + \mathbf{P}/2, \downarrow) \tag{2}$$

Since generally, the single-electron wavefunction has the form of a plane wave $\phi \propto e^{i\mathbf{P}\cdot\mathbf{r}/\hbar}$, and since the additional momentum term $\mathbf{P}/2$ is the same for all terms, the momentum can be expressed as a factor outside the summation in equation 1 such that:

$$\Phi(\mathbf{r}_1, \mathbf{r}_2) = \sum_j a_j \phi(\mathbf{r}_1, \mathbf{P}_j, \uparrow)\phi(\mathbf{r}_2, -\mathbf{P}_j, \downarrow)e^{i\mathbf{P}\cdot\mathbf{r}_1/2\hbar}e^{i\mathbf{P}\cdot\mathbf{r}_2/2\hbar} = \Phi(\mathbf{r}_1, \mathbf{r}_2)e^{i\mathbf{P}\cdot\mathbf{r}/\hbar}, \qquad (3)$$

where $r = \frac{\mathbf{r}_1 + \mathbf{r}_2}{2}$ describes the position of the Cooper pair's center of mass. Expressing the condensate wavefunction like this indicates that the momentum gives rise to a phase of the wavefunction, and since all the Cooper pairs have the same wavefunction, this can be extended to a full wavefunction describing all Cooper pairs in the condensate as $\Psi_P = \Psi e^{i\mathbf{P}\cdot\mathbf{r}/\hbar}$, where Ψ is the complete condensate wavefunction when no current is passing through the superconductor.

For current through a superconducting circuit, the acquired phase along the path of the circuit, connecting two points X and Y, is then given by

$$\Delta\phi_{XY} = \frac{1}{\hbar}\int_x^Y \mathbf{P}(\mathbf{r})\cdot d\mathbf{r} = \frac{m}{en_p}\int_X^Y \mathbf{J}(\mathbf{r})\cdot d\mathbf{r}, \qquad (4)$$

where the last expression is the phase gradient expressed in terms of the current density $\mathbf{J} = \frac{n_p e}{m}\mathbf{P}$, with n_p the Cooper pair density, and e and m the electron charge and electron mass, respectively. If, in addition to this, an external magnetic field is present, an electric field is induced, and the momentum gains a term describing the contribution from the field, such that $\mathbf{P} = m\mathbf{v} + q\mathbf{A} = 2m\mathbf{v} + 2e\mathbf{A}$, where $\mathbf{A}$ is the vector potential, defined by $\nabla \times \mathbf{A} = \mathbf{B}$. The phase gradient in the presence of a magnetic field is then described by:

$$\Delta\phi_{XY} = \frac{m}{en_p}\int_X^Y \mathbf{J}(\mathbf{r})\cdot d\mathbf{r} + \frac{2e}{\hbar}\int_X^Y \mathbf{A}(\mathbf{r})\cdot d\mathbf{r} \qquad (5)$$

If the path of the superconducting circuit is a closed loop C, the fact that the phase of the condensate wavefunction must always be single-valued leads to the requirement that the phase must be an integer multiple of 2π, that is, $\Delta\phi_C = k2\pi$. This means that the phase is *quantized*, and the following will show that the flux and phase are related, leading to the quantization of the flux through the loop. Using Stokes theorem for the integral in the second term of equation 5 (now closed loop integral instead of open path integrals) reveals that it describes the magnetic flux through the loop:

$$\oint_C \mathbf{A}\cdot d\mathbf{r} = \int\int_S \nabla\times\mathbf{A}\cdot d\mathbf{S} = \int\int_S \mathbf{B}\cdot d\mathbf{S} = \Phi_S,$$

4

where S indicates the surface enclosed by C. The so-called fluxoid Φ' can now be defined as

$$\Phi' \equiv \frac{1}{2\pi} \left(\frac{m}{2n_p e^2} \oint_C \mathbf{J} \cdot d\mathbf{r} + \Phi_S \right) = k\Phi_0,$$

where $\Phi_0 = \frac{h}{2e}$ is the superconducting flux quantum, which is related to condensate phase by $\Phi' = \frac{\Phi_0 \Delta \phi_C}{2\pi} = \phi_0 \Delta_C$, where $\phi_0 = \frac{\Phi_0}{2\pi}$ is called the reduced flux quantum. This shows that the total flux threading a superconducting loop must be quantized in multiple integers of the flux quantum, which is an effect that can be used for the so-called SQUID (see section 1.1.3). [5]

An central element in superconducting qubits it the Josephson junction. The Josephson junction consists of two superconducting islands separated by a thin insulating layer, resulting in a potential barrier between the two islands. Given the right conditions, the wave functions of the electrons on either side of the insulating layer crosses the potential barrier and overlaps with the wave function on the other side, resulting in a coupling between the number of electrons on each side of the junction. Because of this, the electrons can tunnel back and forth between the two superconducting islands. The use of the Josephson junction to build qubits is discussed in section 1.1.2.

1.1.2 The transmon qubit

The transmon is a superconducting qubit that can be viewed as a special case of a charge qubit called the Cooper pair box. The Cooper pair box is comprised of circuit with a small superconducting island connected to a large reservoir of Cooper pairs, constituting a Josephson junction. The island should be small enough to only be capacitively coupled to the reservoir and to not interact with anything else in the environment. To be able to perform operations on the system, the Josephson junction is connected to a capacitor that is connected to a voltage source, see Figure 2(a). By varying the voltage source will change the number of charges on the capacitor plates, which then controls the number of charges on the island. In the number basis, the Cooper pair box is described by the Hamiltonian [5]:

$$H = 4E_C(n - n_g)^2 \left| n \right\rangle \left\langle n \right| - \frac{E_J}{2} \sum (\left| n \right\rangle \left\langle n + 1 \right| + \left| n + 1 \right\rangle \left\langle n \right|)$$

The last term describes the tunneling process of Cooper pairs in a Josephson junction. $\left| n \right\rangle$ is the eigenstate of the number operator n which describes the number of Cooper pairs on one of the islands (thereby determining the number of pairs on the other island as well), and E_J is the Josephson energy and describes the coupling between the islands and thereby how much energy is needed to tunnel between them. Since a Josephson junction consists of two layers of two conducting electrodes, which constitute a capacitor,

it can effectively be described as a capacitor of capacitance C_J in parallel with the pure tunneling element. Therefore, to describe an actual Josephson junction, a capacitive term $\frac{(2e)^2}{2C_J} \sum_n n^2 |n\rangle \langle n|$ must be added to the Hamiltonian, describing energy associated with 1 Cooper pair's charge across the capacitor plates. The role of the gate capacitor is then to create a charge offset, and the full capacitive term of the Cooper pair box is then $E_C(n - n_g)^2 |n\rangle \langle n|$, where $n_g = \frac{Q_g}{e}$, and with Q_g the charge across the gate capacitor plates.The charging energy associated with these capacitive elements is then $E_C = \frac{(e)^2}{2(C_g + C_J)}$, with C_g the capacitance of the gate capacitor.

The Cooper pair box is usually operated in the regime $E_C \ll E_J$. Here, the tunnel coupling Hamiltonian can be seen as a perturbation to the $E_J = 0$ case. For no tunneling, $E_J = 0$, the Hamiltonian is diagonal, and the eigenstates are $|0\rangle$, $|1\rangle$ with eigenenergies as a function of n_g plotted in Figure 3(a). Here, the separation from the two lowest energy levels to higher energy level is large, validating the two-level approximation needed for a qubit. In the small tunnel coupling regime, $E_J \ll E_C$, the eigenenergies are approximately the same as for $E_J = 0$. However, as $E_J 0$ and gets larger compared to E_C, the degeneracy between the $n_g = n \pm \frac{1}{2}$ etc. is lifted, and so-called avoided crossings occur, see . This happens because, as E_J becomes larger compared to E_C, the larger the effect of the off-diagonal elements in the Hamiltonian. That is, in the two-level approximation, for $E_J \ll E_C$, the Hamiltonian approaches a matrix with only off-diagonal entries, with eigenstates $|+\rangle$ and $|-\rangle$.

While the Cooper pair box qubit's sensitivity to charge is what gives control over the qubit, it is also a disadvantage. Since the qubit must be sensitive enough that a single electron has a great effect on the energy of the system, this means that the Cooper pair box is also very sensitive to charge noise, which may cause dephasing of the qubit. As a solution to this, one can instead operate the qubit in the so-called transmon regime, $E_C \ll E_J$, where the eigenstates of the system become superpositions of many charge number states, and therefore the sensitivity to a single electron is not as large. This means that the spectrum flattens out, as seen in figure 3. Now, the qubit cannot be controlled via a charge gate/voltage bias, but can instead be controlled by microwave pulses and flux pulses, the latter described in section 1.3. In order to obtain $E_C \ll E_J$, a large capacitor is placed in parallel with the Josephson junction to lower the charging energy (since the charging energy is inversely proportional to capacitance). This circuit can be seen in Figure 2(b).

The transmon Hamiltonian can be written in terms of the phase operator, which is related to the number basis by $e^{i\phi} = \sum |n - 1\rangle \langle n|$ and $e^{-i\phi} = \sum |n\rangle \langle n - 1|$:

$$H = 4E_C n^2 - E_J \cos \phi,$$
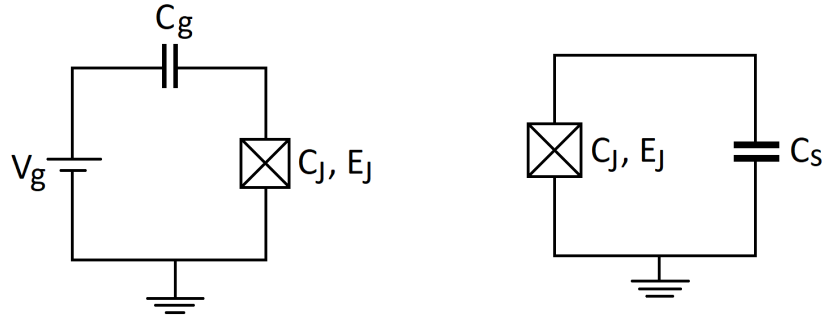
(a) Circuit diagram of a Cooper pair box. The Josephson junction, is connected to a gate capacitor of capacitance C_g, and gate operations are performed by tuning the gate voltage V_g.

(b) Circuit diagram of the transmon qubit. Josephson junction is shunted by a large capacitor of capacitance C_S, ensuring that the qubit is in the transmon regime $E_J \gg E_C$

Figure 2

where now, the charging energy is $E_C = \frac{e^2}{2(C_J+C_S)}$, with C_J and C_S the junction capacitance and shunt capacitance, respectively, and $\phi = \frac{2\pi\Phi}{\Phi_0}$. Taylor expanding the tunneling term $-E_J \cos\phi$ to second order yields $-E_J + \frac{E_J^2(2\pi)^2}{2\Phi_0^2}\Phi^2$. Ignoring the offset $-E_J$ and comparing this to the Hamiltonian for an inductor, $H_{\text{inductor}} = \frac{\Phi^2}{2L}$, one sees that the Josephson junction to lowest order corresponds to an inductor with inductance $L_J = \frac{\Phi_0^2}{E_J^2 4\pi^2}$. Including higher order of the Taylor expansion shows that the Josephson junction acts like a non-linear inductor. This leads to the equivalent description of a transmon as an LC-circuit with a Josephson junction instead of an inductor.

In an LC oscillator, since both the capacitor and inductor are linear elements, the potential energy of the LC circuit as a function of the superconducting phase is a parabola (see Figure 4(a)) with energy levels of the system equidistantly spaced with $\hbar\omega_0 = \hbar\sqrt{8E_L E_C} = \hbar\sqrt{1/LC}$. This even spacing in energy levels is not useable for building a qubit, since one needs an isolated subset of states, such that the system is not unintentionally excited to higher energy levels when performing operations on it. However, by replacing the linear inductor with the non-linear Josephson junction, the energy spacings become differen for each transition, and thus the two lowest energy levels are isolated from higher levels, creating a subspace of levels which can be used as a qubit. The eigenenergies of the transmon Hamiltonian are approximately given by $E_m \simeq -E_J + \sqrt{8E_C E_J}(m + \frac{1}{2}) - \frac{E_C}{12}(6m^2 + 6m + 3)$ [6]. The isolation of the two lowest level of the transmon from the next level is quantified by the anharmonicity $\alpha = \omega_q^{1\to2} - \omega_q^{0\to1} = -E_C$. For large enough anharmonicity, the system can be described

7
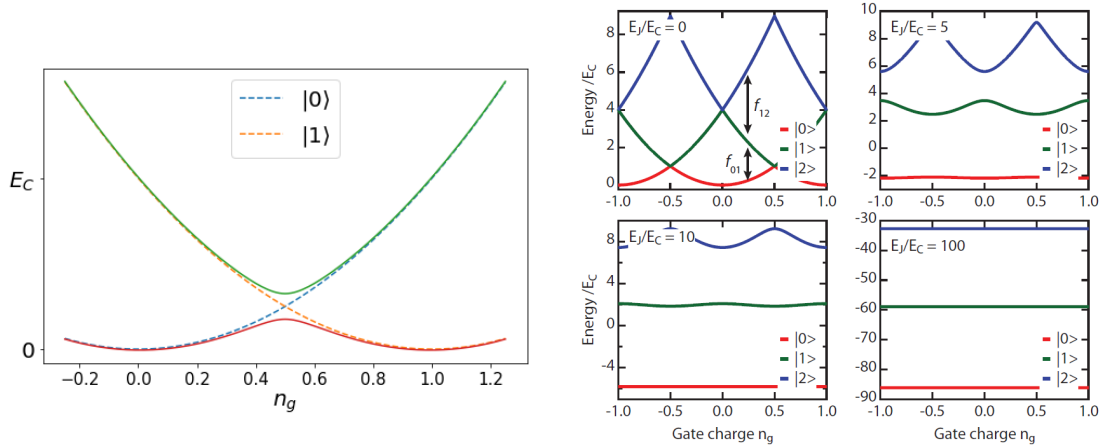
(a) Energies of a Cooper pair box (CPB) qubit as a function gate charge. For $E_J = 0$, the qubit energies are degenerate at $n_g = 1/2$. As E_J becomes non-zero, this degeneracy is lifted, and a so-called avoided crossing occurs instead.

(b) Energies of a CPB qubit as a function of gate charge n_g for different E_J/E_C. As the ratio E_J/E_C increases, the qubit's sensitivity to charge decreases. Figure from [7]

Figure 3

as a two-level system, resulting in the Hamiltonian:

$$H = \frac{f_{01}}{2}\sigma_z \tag{6}$$

with transition frequency $f_{01} = (\sqrt{8E_C E_J} - E_C)/h$. The larger the magnitude of the anharmonicity, the more the two ground levels comprising the qubit are isolated from higher energy levels, which decreases the risk of leakage into non-computational states. However, E_J simultaneously needs to fulfill the requirement of a transmon that $E_C \ll E_J$, and so there is a trade-off between charge noise (in)sensitivity and anharmonicity. Typical values for α are 100-300 MHz , while $E_J/E_C \geq 50$ [3].

1.1.3 Flux-tunable transmons

The transmon described in section 1.1.2 has a fixed transition frequency $f_{01} = (\sqrt{8E_C E_J} - E_C)/h$. For certain qubit operations, discussed in section 1.3, it is necessary to be able to control the qubit frequency, for example to turn on an interaction between two qubits by bringing them into resonance which each other, and turn off this interaction as well. For this purpose, one must be able to tune the qubit frequency of one of the qubits. A way to do this is by replacing the single Josephson junction with a so-called dc-SQUID (superconducting quantum interference device) loop. This consists of a loop
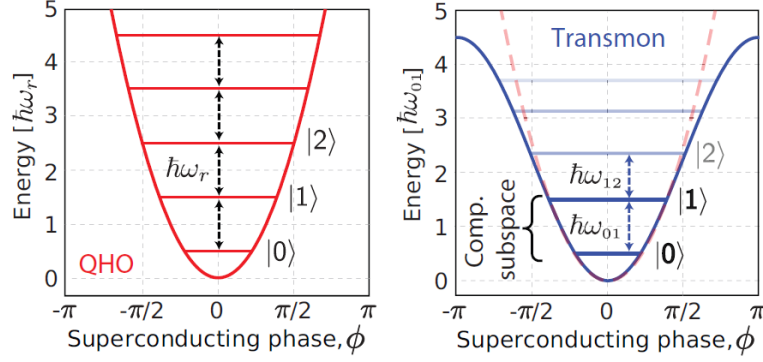
Figure 4: Left: The potential of a quantum LC oscillator. The energy levels are equidistant, with spacing $\Delta_E = \hbar\omega_r$, which means that this system cannot be used as a qubit. Right: The potential of a transmon. Due to the anharmonicity $\hbar\omega12 - \hbar$ Figure from Krantz et al.[3]

with two Josephson junctions connected in parallel. Due to flux quantization, the total flux through the SQUID must be an integer of flux quanta, leading to the following constraint (in terms of phase) [3]:

$$\phi_1 - \phi_2 + 2\phi_e = 2\pi k,$$

where ϕ_i is the phase gain associated with the junctions $i = 1, 2$, $\phi_e = \frac{\pi\phi_{ext}}{\Phi_0}$ is the phase caused by the externally applied magnetic flux through the loop, and k is an integer. The pure tunnelling part of the Hamiltonian describing the Josephson junctions, H_J, now consists of two terms, one for each junction[7][6]:

$$H_J = E_{J1}\cos(\phi_1) + E_{J2}\cos(\phi_2)$$

For $\phi = \phi_1 - \phi_2 = 2\pi\frac{\Phi_{ext}}{\Phi_0}$ and $\theta = \frac{\phi_1 + \phi_2}{2}$, the Hamiltonian can be expressed as:

$$
\begin{aligned}
H_J &= E_{J1}\cos\left(\theta + \frac{\phi}{2}\right) + E_{J2}\cos\left(\theta - \frac{\phi}{2}\right) \\
&= E_{J1}\left[\cos(\theta)\cos\left(\frac{\phi}{2}\right) + \sin(\theta)\sin\left(\frac{\phi}{2}\right)\right] + E_{J2}\left[\cos(\theta)\cos\left(\frac{\phi}{2}\right) - \sin(\theta)\sin\left(\frac{\theta}{2}\right)\right] \\
&= (E_{J1} + E_{J2})\cos(\theta)\cos\left(\pi\frac{\Phi_{ext}}{\Phi_0}\right) + (E_{J1} - E_{J2})\sin(\theta)\sin\left(\pi\frac{\Phi_{ext}}{\Phi_0}\right)
\end{aligned}
$$

Here, the trigonometric identity $\cos(A \pm B) = \cos A \cos B \pm \sin A \sin B$ was used in the second line. If the junctions are identical, such that $E_{J1} = E_{J2}$, the second term vanishes, and H_J is equal to the pure tunneling Hamiltonian of a single transmon, now with the

9

effective junction energy:

$$E_J^{eff} = (E_{J1} + E_{J2}) \cos\left(\frac{\pi\Phi_{ext}}{\Phi_0}\right) \equiv E_J \cos\left(\frac{\pi\Phi_{ext}}{\Phi_0}\right)$$

This leads to a transition frequency given by:

$$f_{01} \approx \frac{1}{h}\left(\sqrt{(8E_C E_J |\cos(\pi\Phi_{ext}/\Phi_0)|} - E_C\right) \tag{7}$$

This means that the transition frequency of the qubit can now be tuned by varying the flux threading the SQUID loop, see Figure 5(a). While this dependence on Φ_{ext} is a tool for implementing wanted frequency tuning, it simultaneously introduces a sensitivity to flux noise. To first order, the sensitivity to flux noise is described by $\frac{df_{01}}{d\Phi_{ext}}$ which is non-zero everywhere except at $\phi_{ext} = k\Phi_0$, for k an integer. This means that when $\Phi_{ext} = \Phi_0$, f_{01} is first-order insensitive to flux noise, and this is referred to as the sweet spot. One should therefore operate at this flux value when idling, i.e. when not performing flux gates. The magnetic flux threading the loop is controlled by using a flux bias line, where a voltage signal generated by an AWG is is converted to a current I via a resistance R, and this current is passed through a wire near the SQUID loop. The mutual inductance M between the wire and the SQUID loop, the magnetic flux threading the loop via $\Phi_{ext} = MI$, see Figure 5(b).
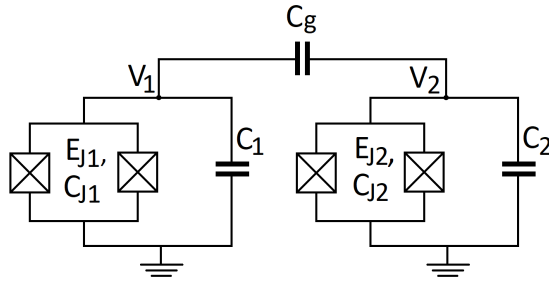
1.2 Coupling of qubits

Figure 6: Schematic showing direct coupling of two flux-tunable transmons via a coupling capacitor with capacitance C_g.

In order to implement quantum algorithms and create entanglement, coupling between qubits is needed. There are various ways to physically implement this coupling, for example via mutual inductance between qubit circuits, or via capacitive coupling. An
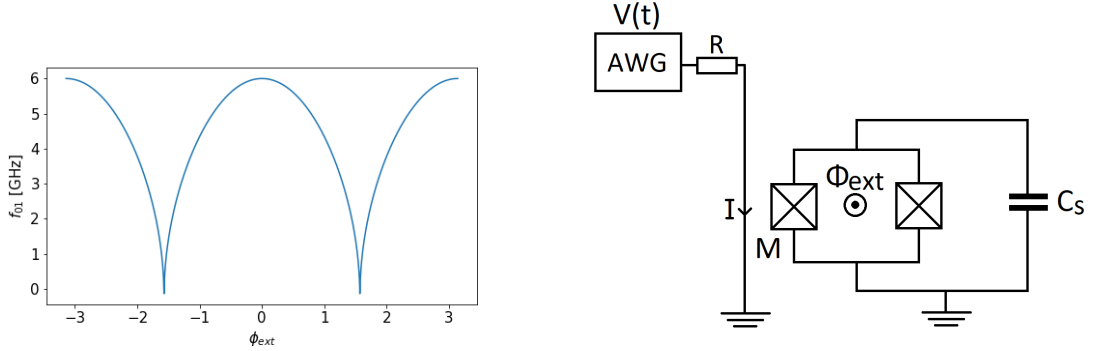
(a) Energy spectrum of a single flux-tunable transmon, where $\phi_{ext} = \frac{\pi\Phi_{ext}}{\Phi_0}$ describes the external flux threading the loop. The energy scales used are $E_C/h = 0.25$ GHz and $E_J/h = 19.5$ GHz

(b) Simple circuit diagram of a flux-tunable transmon and flux bias line. A voltage signal can be generated by an arbitrary waveform generator (AWG), which gives rise to a current in the flux bias line. The mutual inductance M between the flux control line and SQUID loop causes a magnetic flux Φ_{ext} to thread the SQUID loop.

Figure 5

illustration of direct capacitive coupling between to flux-tunable transmons is shown in Figure 6. The qubits are each connected to the coupling capacitor between them, and the coupling is then described by the interaction term H_{int} of the system Hamiltonian $H_{tot} = H_{q1} + H_{q1} + H_{int}$ and is given by[[3]]:

$$H_{int} = C_g V_1 V_2,$$

where C_g is the capacitance of the coupling capacitor, and V_1 and V_2 are the voltage operators of the voltage nodes of each qubit. In the limit $C_g \leq C_11, C_2$, assuming a two-level approximation and using the rotating wave approximation, the full Hamiltonian is then of the form:

$$H = \sum_{i=1,2} \frac{1}{2}\omega_i \sigma_z + g\sigma_{y,1}\otimes, \sigma_{y,2} \tag{8}$$

where g is the coupling rate which depends on the type of coupling used. For direct capacitive coupling, it is given by:

$$g = \frac{1}{2}\sqrt{\omega_{q1}\omega_{q2}} \frac{C_g}{\sqrt{C_g + C_1}\sqrt{C_g + C_2}},$$

11

Rewriting 8 as $H_{int} = -g([\sigma_+ - \sigma_-] \otimes [\sigma_+ - \sigma_-])$, using the rotating wave approximation again), and setting $\omega_{q1} = \omega_{q2}$, i.e. tuning the qubits into resonance, the Hamiltonian reads:

$$H_{int} = g(\sigma_+ \otimes \sigma_- + \sigma_- \otimes \sigma_+) = \frac{g}{2}(\sigma_x \otimes \sigma_x + \sigma_y \otimes \sigma_y) \tag{9}$$

This expression shows how the coupling can give rise to excitations being swapped between the qubits, and this is utilized in the iSWAP gate described in section 1.3.

1.3 Two-qubit gates and flux pulse distortions

As mentioned in the Divincenzio criteria, a universal set of gates is required for quantum computing, and this means that one needs two-qubit gates to be able to implement quantum algorithms. Two types of two-qubit gates will be discussed here, namely the CPHASE (or CZ) gate and the iSWAP gate. For a system of two coupled qubits q_1 and q_2, the possible states are $|00\rangle$, $|01\rangle$, $|10\rangle$ and $|11\rangle$, where $|nm\rangle = |n\rangle_{q1} \otimes |m\rangle_{q2}$. In the basis $|0\rangle = (1\ 0)^T$, $|1\rangle = (0\ 1)^T$, these corresponds to the four state vectors:

$$|00\rangle = \begin{pmatrix} 1 \\ 0 \\ 0 \\ 0 \end{pmatrix}, |01\rangle = \begin{pmatrix} 0 \\ 1 \\ 0 \\ 0 \end{pmatrix}, |10\rangle = \begin{pmatrix} 0 \\ 0 \\ 1 \\ 0 \end{pmatrix}, |11\rangle = \begin{pmatrix} 0 \\ 0 \\ 0 \\ 1 \end{pmatrix}$$

The iSWAP gate is two-qubit gate that swaps excitations between the $|01\rangle$ and $|10\rangle$ states and applies a phase shift of $\pi/2$ ($e^{-i\pi/2} = -i$) to the state, thereby resulting in the name iSWAP [3]:

$$i\text{SWAP} = \begin{pmatrix} 1 & 0 & 0 & 0 \\ 0 & 0 & -i & 0 \\ 0 & -i & 0 & 0 \\ 0 & 0 & 0 & 1 \end{pmatrix} \tag{10}$$

The iSWAP gate can be directly derived from the interaction term describing capacitive qubit coupling (equation 8):

$$H_{int} = g(\sigma_+ \otimes \sigma_- + \sigma_- \otimes \sigma_+) = \frac{g}{2}(\sigma_x \otimes \sigma_x + \sigma_y \otimes \sigma_y)$$

This Hamiltonian gives rise to the unitary operator:

$$U(t) = e^{-iHt} = e^{-i(\frac{g}{2}(\sigma_x \otimes \sigma_x + \sigma_y \otimes \sigma_y)t)}$$

$$= \begin{pmatrix} 1 & 0 & 0 & 0 \\ 0 & \cos(gt) & -i\sin(gt) & 0 \\ 0 & -i\sin(gt) & \cos(gt) & 0 \\ 0 & 0 & 0 & 1 \end{pmatrix}$$

If the two qubits are flux-tunable transmons, the coupling can be turned on by tuning the transmons into resonance for a time t'. For $t' = \frac{\pi}{2g}$, this effectively implements the iSWAP gate, since the cosine elements become zero, and $-i\sin(gt') = -i$, such that $U(\frac{\pi}{2g}) = i$SWAP. To do this in practice, one must apply a (preferably) square flux pulse to one of the qubits - as an example, consider the flux pulse applied to qubit one. This can be done as discussed in section 1.1.3 via the setup in Figure 5(b). The amplitude of the flux pulse must then be arranged such that the qubit makes an excursion to $\Phi_{i\text{SWAP}}$, where the avoided crossing between $|10\rangle$ and $|01\rangle$ is, see Figure 7(a). This means that if the system starts out in the $|10\rangle$ state, and a flux pulse of duration τ is applied, the excitation swaps back and forth between qubit 1 and qubit 2 with a frequency $\frac{1}{2t'} = \frac{g}{\pi}$, see Figure 7(b). In addition to the $-i$ phase shift, the single qubit states obtain a phase

$$\theta_z = \int_0^\tau (\omega_q - \omega(t))$$

during the flux pulse operation. This is a result of the qubit precession around the z-axis of the Bloch sphere which changes as the frequency is tuned. These single-qubit phases afterwards can be cancelled out by single-qubit rotations around the z-axis, such that the full operation is equal to an iSWAP gate.

The unitary operator describing the CPHASE gate is:

$$\text{CPHASE} = \begin{pmatrix} 1 & 0 & 0 & 0 \\ 0 & 1 & 0 & 0 \\ 0 & 0 & 1 & 0 \\ 0 & 0 & 0 & -1 \end{pmatrix} = |0\rangle \langle 0| \otimes \mathbb{1} + |1\rangle \langle 1| \otimes Z, \tag{11}$$

where Z is the Pauli Z matrix. This is a conditional gate, meaning that the operation on qubit 2 (the target qubit) depends on the state of qubit 1 (the control qubit). For the CPHASE gate, this means that a Z-gate is applied to qubit 2 if qubit 1 is in state $|1\rangle$, yielding a phase shift of π ($e^{-i\pi}$=-1) if the coupled system is in state $|11\rangle$, and otherwise, the identity operator is applied, such that no changes are applied to the system.
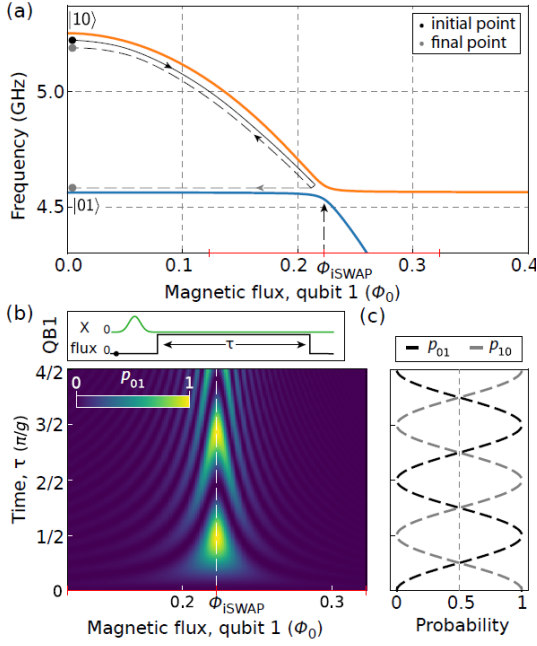
Figure 7: (a) The energy levels of a system of two coupled flux-tunable transmons as a function of the magnetic flux on qubit 1. The trajectory in (Φ, f)-space is indicated by the black an grey arrows: if the intial state is $|01\rangle$, the flux pulse brings the qubit to $\Phi_{i\text{SWAP}}$ and either back along $|10\rangle$ or $|01\rangle$, depending on the duration of the pulse. (b): The population of $|01\rangle$ as a function time and magnetic flux on qubit 1. (c). The probabilities of the qubit populating state $|01\rangle$ and $|10\rangle$, respectively, plotted versus time at $\Phi_{ext} = \Phi_{i\text{SWAP}}$. Figure from Krantz et al.[3]
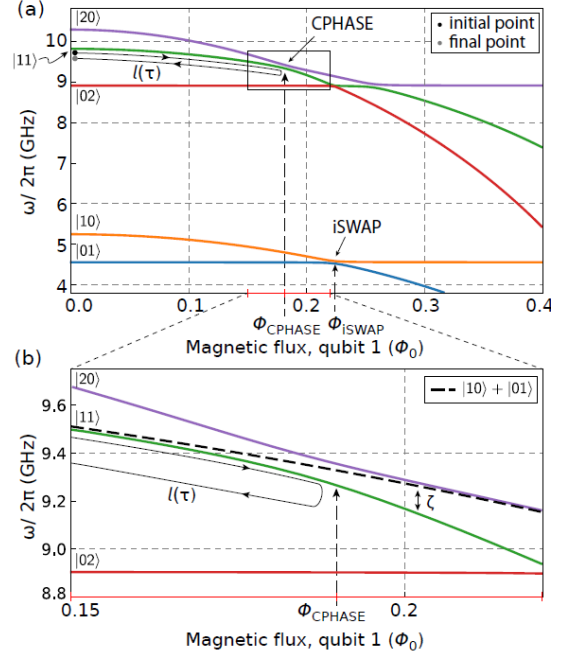
Figure 8: (a) The energy levels of a system of two coupled flux-tunable transmons as a function of the magnetic flux on qubit 1, now including the non-computational states $|20\rangle$ and $|02\rangle$. (b) A zoomed-in view of the avoided crossing between $|11\rangle$ and $|20\rangle$, along with $\omega_{10} + \omega_{01}$ plotted as a dashed line. The CPHASE gate brings $|11\rangle$ to the avoided crossing and back again, resulting in a phase gain of $|11\rangle$. By cancelling out the single qubit phases θ_{nm}, the qubit state effectively gains a phase determined by the difference between ω_{11} and $\omega_{10} + \omega_{01}$ i.e. ζ. Figure from Krantz et al. [3]

The CPHASE gate builds on the same concept as the iSWAP gate, of an excursion to an avoided crossing, only here the avoided crossing is between $|11\rangle$ and $|20\rangle$. This avoided crossing is seen in Figure8, and since the $|20\rangle$ state is outside the computational space, one needs to expand the Hamiltonian to find the energy levels involved. For two excitations present in the system, the Hamiltonian (in the basis $|00\rangle, |01\rangle, |10\rangle, |11\rangle, |02\rangle, |20\rangle$)

is:

$$H_{2exc} = \begin{pmatrix} E_{00} & 0 & 0 & 0 & 0 & 0 \\ 0 & E_{01} & g & 0 & 0 & 0 \\ 0 & g & E_{10} & 0 & 0 & 0 \\ 0 & 0 & 0 & E_{11} & \sqrt{2}g & \sqrt{2}g \\ 0 & 0 & 0 & \sqrt{2}g & E_{02} & 0 \\ 0 & 0 & 0 & \sqrt{2}g & 0 & E_{20} \end{pmatrix}, \tag{12}$$

from where the coupling g between $|11\rangle$ and $|20\rangle$ and $|02\rangle$ is directly seen (scaled by $\sqrt{2}$ because there are two excitations). The energies are the sum of the individual transmon qubit energies, i.e. $E_{nm} = E_n + E_m$. From the eigenenergies of H_{2exc}, the transition frequency from $|00\rangle$ to each state, i.e., $\omega_{nm}/2\pi = \frac{1}{h}(\varepsilon_{nm} - \varepsilon_{00})$, is found and plotted in Figure 8, where ε_{nm} is the eigenenergy of state $|nm\rangle$. By preparing the system in state $|11\rangle$ and applying a flux pulse to qubit 1, bringing the external flux to the avoided crossing between $|11\rangle$ and $|20\rangle$ at $\Phi_{ext} = \Phi_{CPHASE}$ and then waiting for some time τ at the avoided crossing, the states obtain phases described by the matrix representation of the operation[?][3]

$$U = \begin{pmatrix} 1 & 0 & 0 & 0 \\ 0 & e^{-i\theta_{01}} & 0 & 0 \\ 0 & 0 & e^{-i\theta 10} & 0 \\ 0 & 0 & 0 & e^{-\theta_{11}} \end{pmatrix},$$

where the phase gained by state $|nm\rangle$ is $\theta_{nm}(\ell(\tau)) = \int_0^\tau \omega[\ell(t)]$, where is the trajectory in (Φ, ω)-space, and ω_{nm} is the energy/frequency of $|nm\rangle$ as a function of the trajectory. In order to not populate the $|02\rangle$ and thereby leave the computational space of the qubits, the excursion must happen slowly compared to $1/g$. Defining the parameter ζ:

$$\zeta = E_{11} - (E_{01} + E_{10}),$$

one can design a trajectory ℓ_π such that the integral of ζ:

$$\int_0^\tau \zeta(t)dt = \theta_{11} - (\theta_{01} + \theta_{10}) = \pi$$

resulting in the operator:

$$U = \begin{pmatrix} 1 & 0 & 0 & 0 \\ 0 & e^{i\theta_{01}(\ell_\pi)} & 0 & 0 \\ 0 & 0 & e^{i\theta_{10}(\ell_\pi)} & 0 \\ 0 & 0 & 0 & e^{i[\pi+(\theta_{01}(\ell_\pi)+\theta_{10}(\ell_\pi))]} \end{pmatrix}$$

15

By performing single qubit rotations on the qubits around the z-axis afterwards, the phases $\theta_0 1$ and $\theta_1 0$ can be cancelled out, such that only the $|11\rangle$ state gathers a phase of π, and the operation constitutes an CPHASE gate. Aanother approach than adiabatic excursion is to suddenly bring the qubit to Φ_{CPHASE} and wait for $t = \frac{\pi}{\sqrt{2}g}$. With this method, the $|11\rangle \leftrightarrow |20\rangle$ coupling results in the making a full oscillation, populating the $|20\rangle$ and then returning to $|11\rangle$.

1.4 Qubit relaxation

A challenge in quantum computing is the loss of coherence, setting an upper limit for the duration of quantum gates and the depth of quantum circuits. Decoherence results in a loss of information, and is due to coupling of the qubit to the surrounding environment. Qubit decoherence can be divided into two main categories: decay of the qubit from its excited state $|1\rangle$ to the ground state $|0\rangle$, referred to as energy relaxation or amplitude damping, and dephasing, where information about the phase of the qubit is lost [5].

Energy relaxation happens on a timescale T_1 or at a rate $\Gamma_1 = \frac{1}{T}$ and is caused by the qubit interacting with resonant modes of the environment, leading to energy dissipation. The rate of phase decay has two contributions and is given by $\Gamma_2 = \frac{1}{T_2} = \frac{\Gamma_1}{2} + \Gamma_\phi$, from which it can be seen that T_2 is limited by T_1. Γ_ϕ describes the pure dephasing, which is the dephasing rate if there were no limitation by T_1. Dephasing is caused by dispersive interactions with the environment, which do not result in energy dissipation, but are manifested in small, random kicks in phase and thereby fluctuations in the qubit frequency. The reason that T_2 decay is limited by T_1 is that energy relaxation eventually leads to the Bloch vector pointing directly up (to the $|0\rangle$ state), which is also a process where phase information is lost, thereby resulting in contributions from both types of decoherence.[3]

The evolution of an open quantum system, i.e., a system coupled to the environment, can be described by the Lindblad master equation. To incorporate energy relaxation and dephasing into this description of the system dynamcis, the Lindblad, operators (also referred to as collapse operators) are used. These operators are $\frac{1}{\sqrt{T_1}}a$ and $\frac{1}{\sqrt{2T_2}}\sigma_z$, and describe energy relaxation and dephasing, respectively, where a is the annihilation operator, and σ_z is the Pauli z matrix.[22]

1.5 Qubit readout

In order to perform measurements and algorithms, one must be able to determine the state of the qubit. Readout of the qubit state is performed by coupling the qubit to a superconducting resonator, and the Hamiltonian describing this qubit-resonator system
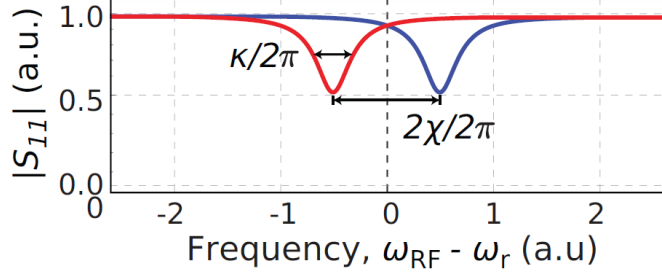
Figure 9: The magnitude of the reflection parameter $|S_{11}|$ after probing a resonator dispersively coupled to a qubit with a signal of frequency ω_{RF}. The red curve is for the qubit in state $|1\rangle$, and the blue is for the qubit in state $|0\rangle$. The dispersive shift of the resonator frequency due to qubit state can then be seen by the location of dips in $|S_{11}|$. Figure borrowed from Krantz et al.[3]

is the Jaynes-Cummings Hammiltonian which is given by [7]

$$H = \omega_r(a^\dagger a + \frac{1}{2}) + \frac{\omega_q}{2}\sigma_z + g(\sigma_+ a + \sigma_- a^\dagger), \tag{13}$$

where the first term describes the resonator Hamiltonian with ω_r the resonator frequency, and a, $a^\dagger$ creation and annihilation operators. The second term describes the qubit, a two-level system with transition frequency ω_q, and the third term describes the qubit-resonator coupling, where g is the coupling rate, and σ_+ and σ_- represents excitation and de-excitation of the qubit, respectively. The limit where the detuning Δ between the resonator frequency and the qubit frequency is large compared to g, i.e. $\Delta = |\omega_q - \omega_r| \gg g$ is called the dispersive regime. Here, energy exchange between the qubit and resonator is suppressed, in comparison to resonant coupling, where excitations are swapped back and forth between the two systems. Although the qubit and resonator now do not directly exchange energy, they do affect each other by shifting each other's frequencies. This is seen by rewriting the system Hamiltonian from equation 13 using second-order perturbation theory in terms of g/Δ and approximating a low-photon limit, which results in[3]:

$$H_{disp} = (\omega_r + \chi\sigma_z)\left(a^\dagger a + \frac{1}{2}\right) + \frac{\tilde{\omega}_q}{2}\sigma_z, \tag{14}$$

where $\chi = \frac{g^2}{\Delta}$ is referred to as the dispersive shift. From this expression, it can be seen how the resonator frequency is effectively shifted from ω_r to $\chi\sigma_z$, demonstrating how the resonator frequency now depends on the state of the qubit: if the qubit is in state $|1\rangle$, the resonator frequency is shifted down by χ, and if it's in state $|0\rangle$, it is shifted up by χ.

17

The qubit frequency is also shifted by an amount $\frac{g^2}{\Delta}$ such that $\tilde{\omega}_q : \omega_q + g^2/\Delta$, which is due to vacuum fluctuations in the resonator. However, this shift is not state-dependent and therefore not a part of the mechanism behind dispersive readout.

Since the shift in resonator frequency can now be mapped to a qubit state, readout can be performed by probing the readout resonator with a signal of frequency ω_{RF}, and analyzing either the transmission through or reflection off the resonator, from where the shift can be found, and the qubit state inferred, see Figure 9 where the reflection $|S_{11}|$ is inspected as a function of probe frequency.

1.6   Cryoscope

As should be clear from section 1.3, being able to apply flux pulses in order to tune the qubit frequency is essential for performing iSWAP and CPHASE gate in flux-tunable transmons. As mentioned in section 1.1.3, the flux pulse is implemented by generating the pulse with an AWG and passing it down the control line. However, various electrical components on the control line give rise to distortions of the signal, and these distortions can severely affect the performance of operations applied to the qubit. For example, for a flux pulse constituting a CPHASE-gate, short-timescale distortions can cause leakage into the $|20\rangle$ state, while long-timescale distortions can affect the repeatability of pulses, when distortions of one pulse affects the following pulse. In this project, such pulse distortions are investigated, characterized and predistorted a simple setup consisting of an AWG, a bias tee and oscilloscope. In this room temperature setup, the pulse distortions can be directly observed on the oscilloscope, and can be predistorted from there. However, in a setup with an actual qubit inside a cryostat, these distortions are not so easily observed, since the distortions are temperature dependent and must therefore be characterized in the cold. In order to characterize and correct for these distortions, the qubit itself is used via the method Cryoscope (short for cryogenic oscilloscope) introduced by Rol et al. [1] The cryoscope method consists of a Ramsey-like experiment where a flux pulse of variable duration $\tau + \delta\tau$ is embedded between two $\frac{\pi}{2}$-pulses separated by T_{sep}, see Figure 10. The goal is to obtain an estimate $\Phi_{R,\tau}(t)$ of the magnetic flux $\Phi_{Q,\tau}(t)$, thereby reconstructing the waveform of the flux pulse.

For this project, as well as in Rol et al.[1], the type of qubit under consideration is a flux-tunable transmon, but the method is applicable for any qubit that has a dependence on the control variable that is quadratic or of higher power and a sweet spot with at least first-order insensitivity to the control variable. At the beginning of the experiment, the qubit is prepared in state $|0\rangle$, and the qubit frequency is biased by a DC current at the
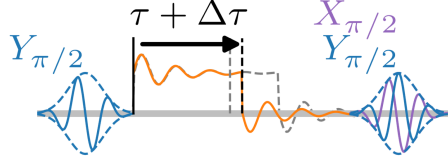
18

Figure 10: Pulse scheme for the cryoscope experiment. A $Y_{\pi/2}$ pulse is applied to the qubit in $|0\rangle$, and a flux pulse of duration $\tau + \Delta tau$ is then applied. The experiment is then ended with two variations: either an $X_{\pi/2}$
    or another $Y_{\pi/2}$ is applied, such that $\langle\sigma_y\rangle$ and $\langle\sigma_x\rangle$ can be measured.

sweet spot $\Phi_{ext} = 0$, cancelling unwanted flux offsets. The experiment then begins with a $\pi/2$-pulse around the Y-axis on the Bloch sphere, such that the qubit is now in state $|+\rangle = \frac{1}{\sqrt{2}}(|0\rangle + |1\rangle)$. Afterwards, a flux pulse of duration $\tau + \Delta tau$ is applied, with Δtau variable, detuning the qubit frequency to some flux value depending on the amplitude of the pulse.During the application of this pulse, the qubit will gain a relative phase, such that its state evolves into $\frac{1}{\sqrt{2}}(|0\rangle + e^{i\phi_\tau}|1\rangle)$, with ϕ_τ given by:

$$\phi_\tau/2\pi = \int_0^\tau \Delta f_Q(\Phi_{Q,\tau}(t))dt + \int_\tau^{T_{sep}} \Delta f_Q(\Phi_{Q,\tau}(t))dt, \tag{15}$$

where the phase is explicitly divided into two contributions: one from the pulse beginning and up to the truncation point, and another resulting from a turn-off transient of the pulse. At a fixed time, T_{sep}, a second $\pi/2$-pulse will be applied, either around the X- or Y-axis of the Bloch sphere, and the state of the qubit is then measured. From this, the $\langle X\rangle$ and $\langle Y\rangle$ Bloch components, and from there ϕ_τ, can be determined. For a short interval, $\tau + \Delta tau$, the average detuning can be estimated by:

$$\overline{\Delta f_R} \equiv \frac{\phi_{\tau+\Delta tau} - \phi_\tau}{2\pi\tau} = \frac{1}{\Delta tau}\int_\tau^{\tau+\Delta tau} \Delta f_Q(\Phi_{Q,\tau+\Delta tau}(t))dt + \varepsilon$$

Here, ε is the inaccuracy of the estimate given by:

$$\varepsilon = \frac{1}{\Delta tay}\left(\int_{\tau+\Delta tau}^{T_{sep}} \Delta f_Q(\Phi_{Q,\tau+\Delta tau}(t))dt - \int_\tau^{T_{sep}} \Delta f_Q(\Phi_{Q,\tau}(t))\right)$$

which is the difference in phase contributions from the two turn-off transients. From the estimated frequency detunings, the pulse shape can be reconstructed in terms of frequency, or in terms of flux by inverting the expression for the transition frequency of a flux-tunable transmon (Equation 7). In this thesis, a simulation of the cryoscope method is performed, however with an alternative method of pulse reconstruction, see

section 3.

2 Predistortion of bias tee pulse at Room temperature

2.1 The sampling theorem

An important concept of signal generation and sampling is the so-called Nyquist (or Shannon) sampling theorem. This theorem states that in order to properly sample a signal, a minimum sampling rate of twice the maximum frequency component in the signal is needed. By proper sampling is meant that the digital signal can be accurately reconstructed, that is, converted back to analog, from the samples.

This means that when converting a continuous (analog) signal to a digital one, minimally two samples per cycle must be obtained. If this requirement is not fulfilled, so-called aliasing will occur, and information is lost. The name aliasing refers to when the sampling rate of a signal is too low, such that the recorded frequency will line up with a slower frequency, see Figure 11. The maximum frequency that can be accurately sampled is referred to as the Nyquist frequency, that is $f_{Nyquist} = S_r/2$, where S_r is the sampling rate. Correspondingly, the Nyquist rate $S_{Nyquist}$ is defined as two times the largest frequency component of the signal. When the largest frequency component of a signal is above the Nyquist frequency, the recorded frequency will be mapped to a frequency between 0 and the Nyquist frequency. This can be demonstrated by generating a signal (here, a sine wave modulated with a Gaussian) and sweeping the frequency of it from below to above the Nyquist frequency and inspecting the Fourier transform of the signals. This was done with an AWG with sampling rate 1.2 GHz, corresponding to a Nyquist frequency of 600 MHz. The result of this can be seen in Figure 12(a), where the Fourier transform is plotted for each of the attempted signal frequencies. When the pulse generator frequency passes 600 MHz, the recorded frequency decreases instead of following the pulse generator frequency. The general pattern of the aliasing can be seen in Figure 12. As seen here, whenever the frequency of the signal is above $f_{Nyquist}$, it is mapped to a digital frequency between 0 and the Nyquist frequency. This means that high frequencies cannot be accurately measured, but also that information about low frequencies will be lost, since the high frequency components that are incorrectly mapped will add to any low frequency components already in the signal. As shown in Figure 11, undersampling can also lead to phase shifts of the signal. These phase shifts are discrete and can only be 0 or 180°, and the pattern of this is shown in the lower part of Figure 12(b).

The sampling theorem can be intuitively explained by considering a an analog, and thereby continuous, signal as seen in Figure 13a with a spectrum as shown in Figure
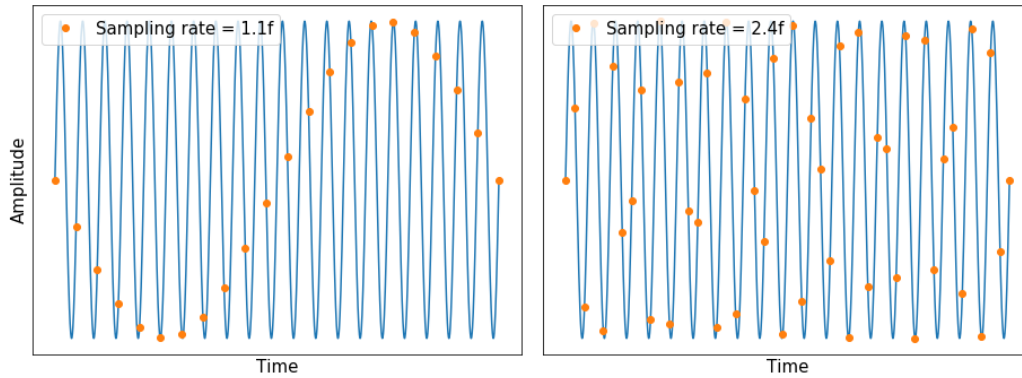
Figure 11: Left: For a sampling rate below the Nyquist rate, the sampled signal can suffer from aliasing, where the frequency is mapped to a lower frequency than that of the signal. In addition to the mismapping of frequency, the sampled signal has gained a phase shift of 180°. Right: The sampling rate is now above the Nyquist frequency, and the signal is appropriately sampled such that no aliasing occurs.
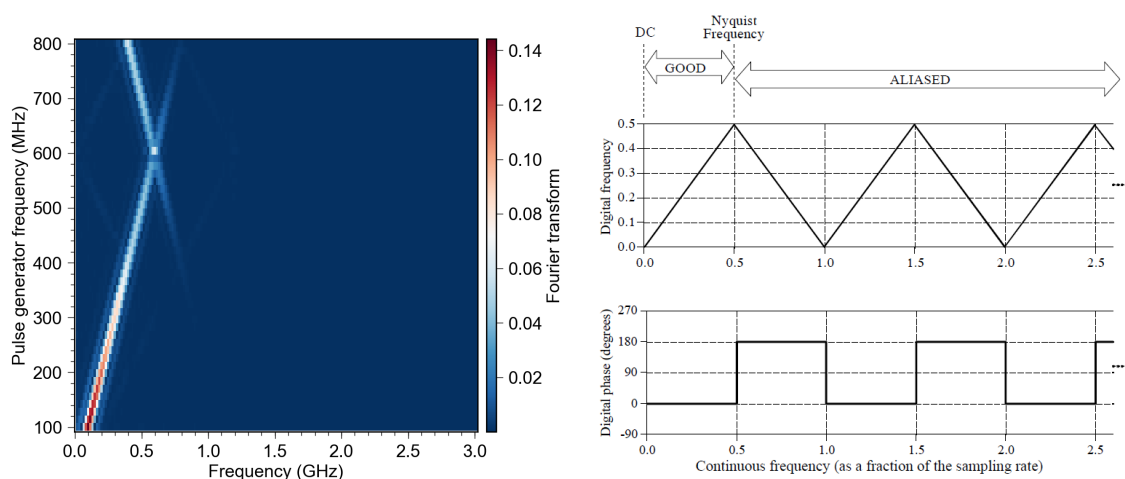
(a) The Fourier transform of signal of increasing frequency. As the Nyquist frequency of 600 MHz is passed, the frequency is mismapped to lower frequencies.

(b) The general pattern of aliasing. If the frequency of a continuous signal is larger than half the sampling rate, the frequency is mapped to a frequency between 0 and the Nyquist rate. Discrete phase shifts of the sampled signal can occur as well. Figure from [10]

Figure 12

13b. Sampling of this signal can be represented by multiplying the signal with a comb function, or impulse train, which is a function that consists of a sum of Dirac delta functions: $\text{comb}(t) = \sum_n \delta(t - n)$ [12], where n corresponds to the equally spaced times at

21

which the signal is sampled. In Fourier space, the comb function is still a comb function, and thus, the Fourier transform of the signal is repeated and mirrored with a periodicity determined by the sample rate. This sampling representation and the corresponding Fourier transform for a sampling rate at 3 times the highest frequency component can be seen in Figure 13(c) and (d). Figure 13(e) demonstrates the same example for a lower sampling rate, namely 1.5 times the highest frequency component in the signal, and the resulting Fourier transform of the sampled signal is shown in Figure 13(f). Here, it can be seen how the signal spectra now overlap, interfering with the single spectrum and thus resulting in a loss of information.

As mentioned, proper sampling is defined by being able to exactly reconstruct the original signal from the sampled signal. When generating a continuous signal with an AWG, digital-to-analog conversion is performed, and so, one "starts from the sampled signal", i.e. the AWG generates an analog signal from a digital (discrete) one. The sampling theorem then comes into play when the sampling rate of the AWG limits the possible frequency range of the generated signal

2.2 AWG calibration

Before simulating the cryoscope method to reconstruct pulses, a characterization of time scales in various bias tees and according predistortion is performed in a simple room temperature setup. However, when examining signal distortion, distortions caused by the AWG itself must be taken into consideration as well. Therefore, before characterizing distortions in the bias tees, the distortions due to the AWG must be investigated through a control setup. In this setup, a pulse with a small Gaussian rise and a plateau, resembling a square pulse, is generated by the AWG and passed directly to an oscilloscope through two coaxial cables connected by an adapter, see Figure 14. These two cables are of the same length and type as the two cables which are later used to connect the AWG to the bias tee and the bias tee to the oscilloscope.

The AWG performance is inspected by doing a sweep of values of the Gaussian width of the control signal and observing how well the AWG generates the signal. The AWG used for this is Textronix AWG5014C with a sample rate of 1.2 GS/s, and according to the sampling theorem, the highest frequency component present in the signal must be half of the sampling rate, i.e., 600 MHz. If this is not fulfilled, the AWG should not be able to accurately generate the signal. To see this limitation in practice, a fine sweep of 50 experiments was done with the width of the Gaussian varied from 100 ps to 5 ns, and with a plateau of 10 ns. In order to reduce the effects of noise, the oscilloscope data in each experiment is averaged 1000 times. For every experiment, a Fourier transform of the signal was done, both for the ideal trace generated in the pulse generator and for the
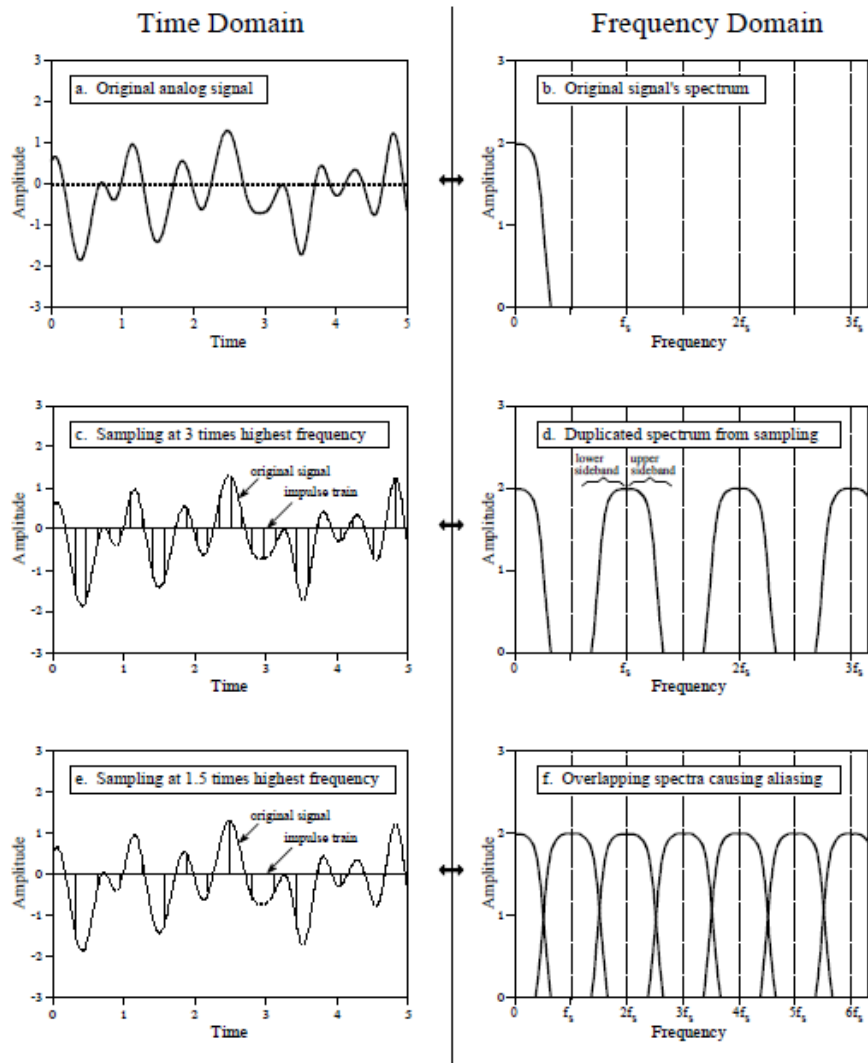
22

Figure 13: Sampling above and below the Nyquist rate visualized in the time domain and frequency domain. Figure from [10]

.

actual signal trace generated by the AWG and passed through the cables in the control setup. The spectrum of the ideal pulse in the first and last experiment is shown in Figure 15. As the width increases, the shape of the pulse goes from being approximately a square pulse, corresponding to a sinc function in Fourier space, to a more Gaussian-like shape. The Fourier transform of a Gaussian is still a Gaussian, which explains why the right plot of 15 shows a more Gaussian-like spectrum with fewer off-center peaks. However, the pulse does of course also include a plateau, so the Fourier transform will never be completely equal to that of a regular Gaussian function. The result is that the

23
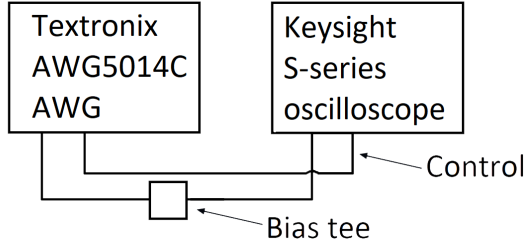
Figure 14: Schematic of the room temperature setup. The signal generated by the AWG is passed either directly to the oscilloscope, or through the bias tee.

larger the width, the narrower the frequency range. Figure 16(a) is a 3D plot showing
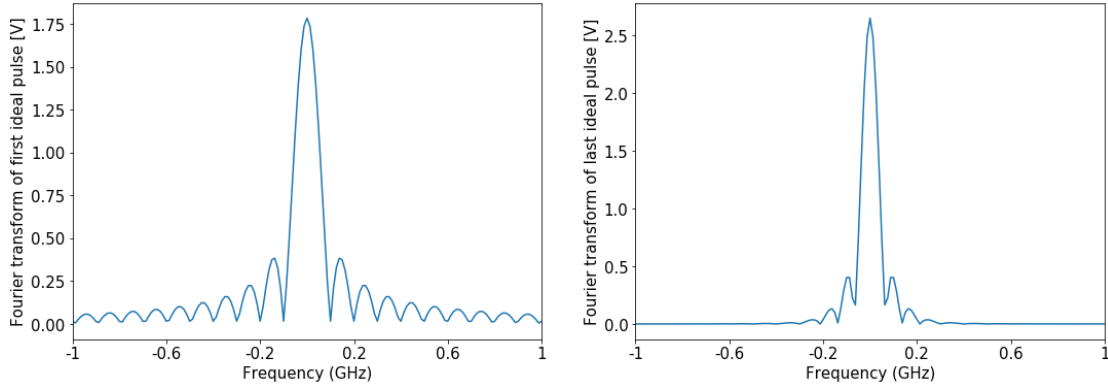

Figure 15: Spectrum of ideal trace in first (left) and last (right) experiment, i.e. for widths 100 ps and 5 ns, respectively.

the spectrum of the ideal pulse in each experiment. Here, it can be seen how the range of frequencies gradually decreases as the width increases. Note that this plot has been normalized in order to improve visibility of the peaks at non-zero frequencies. Following the same procedure for the control pulses yields the results in Figure 17. The shapes of the Fourier transforms are generally the same as in Figure 15, but the range of frequencies is suppressed. As can be seen, the right plot looks very similar to the right plot of Figure 15, which is in good agreement with the fact that the largest frequency component is smaller than the Nyquist frequency. However, the left plot of Figure 17, shows suppression of the peaks at larger frequencies, compared to the left plot of Figure 15. The suppression of the peaks is already present a little below and dominates above the Nyquist frequency at 600 Mhz which is marked with dashed red lines. This decreased range of frequencies can also be seen in Figure 16(b) and suggests that the distortion of the pulse due to the sampling rate of the AWG should disappear at some width where the
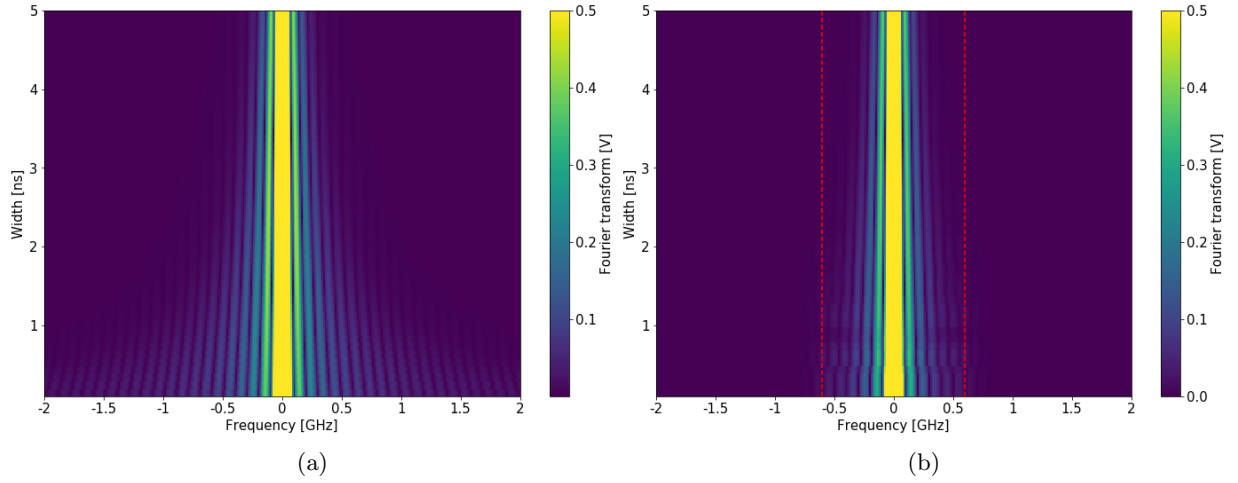
24

Figure 16: (a) Normalized Fourier transform of ideal pulse as function of width. For every experiment, the frequency range needed to generate the pulse decreases (b) Normalized Fourier transform of control pulse as function of width. The red lines mark 600 MHz, which is the Nyquist frequency, and above this absolute value, the magnitude of the peaks declines drastically, demonstrating the sampling theorem.
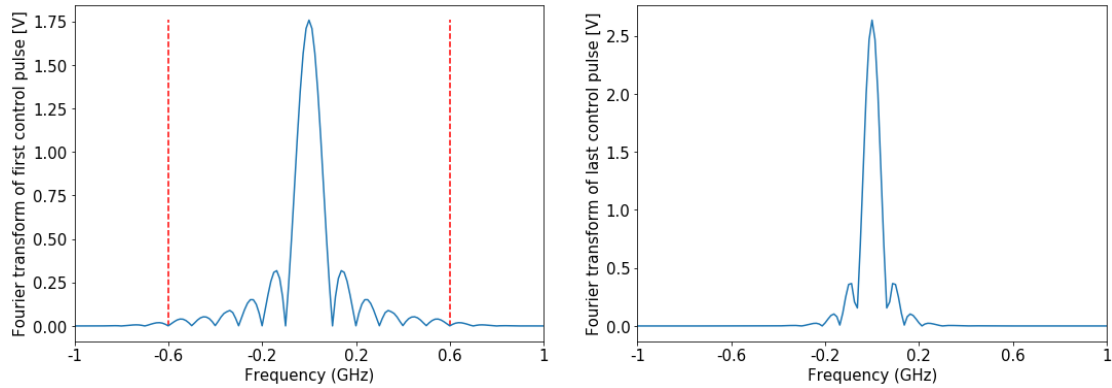

Figure 17: Spectrum of control pulse in first (left) and last (right) experiment, i.e. at width 100 ps and 5 ns, respectively. The dashed red lines mark the Nyquist Frequency, at $\pm$ 600 Mhz

generated pulse does not have any frequency components outside the $\pm$ 600 MHz range. This width could be estimated from Figure 16(b), but in order to have a measure of the discrepancy between the control pulse and the ideal pulse, various ways of quantifying the distortions are explored. Before that is done, however, the pulses must be aligned properly in order to compare them. The first and last sets of data in the width sweep is seen in the left and right plot of Figure 18, respectively. In the left plot, the first thing

25

to note is the ripples present as the pulse rises to its full amplitude and again when it decreases back down to zero. These features are not present in the right plot, but there is still some distortion of the pulse shape, primarily in the form of a noticeable rise time. This type of distortion may be due to the AWG, and possibly the cables and adapter between them. The right plot of Figure 18 shows a time delay between the pulses. This
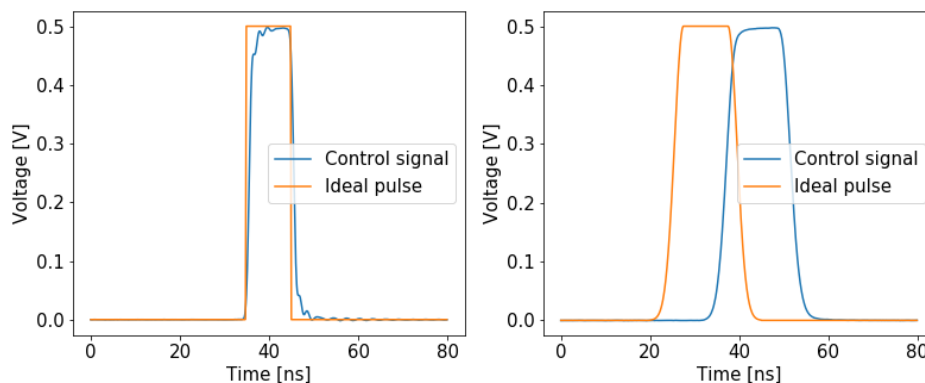

Figure 18: Traces of control pulse and ideal pulse for a Gaussian width of 100 ps (left) and 5 ns (right).

delay arises due to the fact that in the oscilloscope, the start of the pulse is defined by the trigger level, but for the pulse generator, the start of the pulse is defined by the fist non-zero value of the signal. Therefore, as the width of the Gaussian rise increases, the pulses are shifted in time relative to each other, and so, a correction for this delay is needed before subtracting them. As a measure of how well the pulses are aligned, the integral of the absolute difference between the pulses is evaluated as the ideal signal in each plot is shifted to the right point by point. At the optimal alignment, the integrated absolute difference will reach a minimum, and the control signal is then by shifted by the corresponding number of points.

Now, the integrated absolute difference between the control signals and time-corrected ideal signals, i.e. the area between the pulses, is then evaluated for each experiment, and this measure is plotted as a function of width (see upper left plot in Figure 19). Three other methods of quantifying the match of the control pulse to the ideal pulse are plotted as well, namely the dot product between the two data arrays, normalized to the norm of the arrays, as well as the maximum and mean absolute difference between the signals, respectively. All four methods generally show the same trend, namely that the graphs seem to fall off (or grow, in case of the dot product) more slowly above a width of approximately 3 ns. This width is then defined as the optimal width for the square-like pulses, yielding a pulse with all frequency components inside the range allowed by the

AWG. As can be seen from Figure 19, the various methods all continue to yield even better results for widths larger than 3 ns, but since a square pulse is what is really desired, the optimal width should be as small as possible. This prioritization of a short rise time is due to the short qubit lifetime, establishing the need for as fast operations as possible. The integrated absolute difference between a pulse and the ideal pulse is chosen as the standard measure of discrepancy between pulses. This measure will be referred to as integrated absolute difference, deviation or cost function.
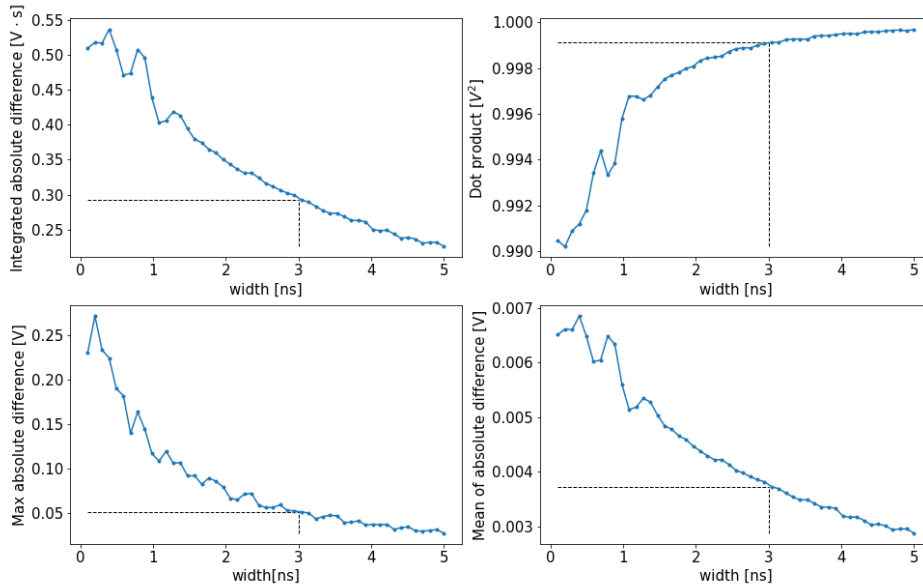

Figure 19: Various methods of quantifying discrepancy between ideal trace and control pulse trace as a function of width. Top left: integrated absolute difference between traces. Top Right: Dot product between the trace data arrays, normalized to the norms of the arrays. For identical pulses, and thereby identical data arrays, the normalized dot product should be equal to one. Bottom left: Maximum absolute difference between traces. Bottom right: The mean of the absolute difference between traces. All methods show approximately the same trend: at and above a width of approximately 3 ns, the curve seems to exhibit less fluctuations and to decrease/rise slower than for smaller widths.

2.2.1 Bias tee circuits and characteristic time scales

A bias tee is a three-port device that in its simplest form consists of a capacitor and an inductor, combined as in Figure 20(a). Port 1 is used for the input AC (or radio frequency) signal, and the DC offset is input in port 3, such that the two signals are combined in port 2. The capacitor blocks direct current, and the inductor blocks alternating current, such that there is no leak between port 1 and 3.
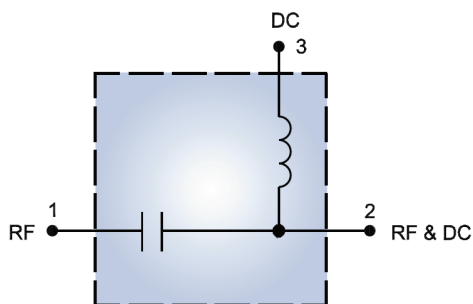
(a) Schematic of the simplest version of a bias tee. Figure from [16].
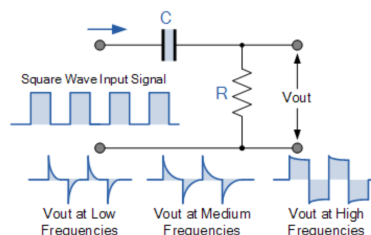
(b) An RC circuit, constituting a high-pass filter. For a square wave input, the amplitude of the pulse decays on a timescale depending on frequency. Figure from [19]

Figure 20

Real wideband bias-tees, however, are made of complex RLC networks, and calculating the characteristic timescales in a bias tee is not a straight-forward task, and it cannot be done from the capacitance and inductance values alone [13]. The primary reason for the complexity of the circuits is the need to circumvent parasitics such as parasitic resonance and capacitance which, for high frequencies, have a large effect on the performance of the bias tee. For example, an inductor can be effectively be described by an equivalent circuit that includes capacitance between the windings as well as resistance in the wires. Similarly, the capacitor has parasitic inductance and reactance which can also be described by an equivalent circuit. This parastic capacitance in an inductor and parasitic inductance in a capacitor have increasingly larger effects as the frequency of the signal through the element is increased. Above the resonance frequency $\omega = \frac{1}{LC}$ (where L is inductance, and C is capacitance), the inductor starts behaving more like a capacitor than an inductor, and the capacitor starts behaving like an inductor [14]. As a result of these parasitics, and the complex designs needed to avoid their effects, the number of timescales and values of these can therefore not be calculated analytically, but need to be extracted directly from fitting the bias tee data.

28

However, if the simple circuit representation of a bias tee in Figure 20(a) is assumed to effectively describe the more complicated bias tee circuits, then only using the RF port and RF+DC port. the bias tee should then constitute a first-order RC high pass filter as seen in Figure 20(b) [21]. The characteristic timescale for such a circuit is $\tau = RC$[17], and the step response is given by $V(t) = V_S + (V_0 - V_S)e^{-t/\tau}$ [20], where R is the resistance and C is the capacitance of the circuit elements. V_S is the amplitude of the step input, and V_0 is the voltage between the capacitor plates when the step input is turned on. The voltage output of a first-order high pass filter is given by[19]

$$V_{out} = \frac{R}{\sqrt{R^2 + X_C^2}} V_{in} = \frac{R}{Z} V_{in},$$

where R is the resistance of the resistor, and X_C is the reactance of the capacitor. Since for an input signal of frequency f, the reactance of a capacitor with capacitance C is given by $Z = \frac{1}{2\pi f C}$, and the resistance R is independent of frequency, the impedance $Z = \sqrt{R^2 + X_C^2}$ is inversely proportional to f. This means that low frequencies are suppressed, and that high frequencies are passed, resulting in a high pass filter. Passing a square pulse through a high pass filter results in the output voltage waveforms seen in Figure 20(b), with the amplitude of the pulse decaying at a timescale set by RC.

In conclusion, the characteristic timescales of the bias tees cannot be predicted exactly. This is first of all due to the lack of knowledge about the exact circuit designs and the fact that the timescales cannot be calculated directly from the capacitance and inductance. Furthermore, even if the this was the case, the capacitance and inductance values of the bias tees are not published. Both the characteristic timescales and number thereof are therefore unknown. This challenge should however also be the case when considering a more complex setup with a flux bias line with more elements, such as amplifiers, filters etc. Being able to predict all the characteristic timescales of the distortions on such a system is most likely not realistic, and therefore, the following fitting procedure and the challenges associated with is should be representative of more general systems.

2.3   Time domain characterization of bias tees

The pulse distortions caused by bias tees can now be characterized. Four different bias tees are analyzed: Mini Circuits ZFBT-6GW+, Mini Circuits ZFBT-4R2GW-FT and Anritsu SC17771, and a QDev e-shop fabricated bias tee, which will be referred to as QDev bias tee. The characterization process of is described in detail for one of them, namely the Mini Circuits ZFBT-6GW+.

The Mini Circuits ZFBT-6GW+ bias tee output for an input pulse with a width of 3 ns,

a plateau of 500 ns and an amplitude of 500 mV, is shown in Figure 21(a). The pulse data is averaged 1000 times, and the trace of the input is plotted as well for comparison. The distortions of the pulse are expressed in a rise time that is slow compared to the ideal pulse, and a decay of the pulse amplitude. This amplitude decay resembles the voltage output waveforms shown in Figure 20(b) for a square pulse input to a high pass filter.

The pulses in Figure 21 are aligned at an artificial trigger level set as low as possible. This trigger level is based on the mean value of the noise in the systm before the pulse begins. This way of aligning the pulses is to include delays of the output signal, and the trigger level of the averaged data can be set lower than the actual trigger level of the oscilloscope in a single measurement. The deviation of the distorted pulse from the ideal pulse is seen in Figure 21(b). The shaded area represents the contribution to the cost function.
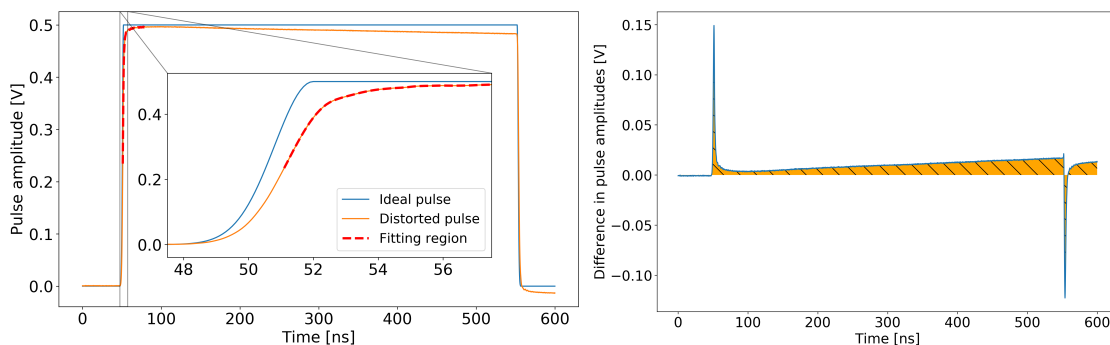
(a) Traces of the ideal pulse and the distorted pulse data from the Mini Circuits ZFBT-6GW+

(b) The trace of the distorted pulse subtracted from the trace of the ideal pulse. The shaded area shows the area between the pulses and is used as a measure of the deviation of the distorted pulse from the ideal pulse.

Figure 21

The distorted signal $s_{out}(t)$ can be described by a convolution of the input signal $V_{in}(t)$ with a function $H(t)$: $s_{out}(t) = H(t) * s_{in}(t)$ [1]. In Fourier space, this corresponds to the multiplication:

$$s_{out}(\omega) = H(\omega)s_{in}(\omega),$$

where $H(\omega)$ is given by [9]:

$$H(\omega) = 1 + \sum_{n=1} \frac{iA_n\omega\tau_n}{i\omega\tau_n + 1} \tag{16}$$

30

In the time domain, this should lead to a pulse shape $s_{out}(t)$ described by:

$$s_{out}(t) = A_0 \left(1 + \sum_{n=1} A_n \cdot \exp(-t/\tau_n) \right) \tag{17}$$

Here, A_0 is some amplitude offset, τ_n are the characteristic timescales describing the distortions, and A_n are the coefficients describing the magnitude of these distortions. In order to find the A_n and τ_n that describe the distortions, the expression for $s_{out}(t)$ can be fitted to the part of the bias tee pulse where the distortions are most pronounced. The ideal waveform $s_{in}(t)$ should then be obtained by deconvolution of $s_{out}(t)$ with $H(t)$:

$$s_{in}(t) = H(t)^{-1}(t) * s_{out}(t),$$

or equivalently, in Fourier space:

$$s_{in}(\omega) = \frac{s_{out}(\omega)}{H(\omega)}$$

This can be done in by using the Predistortion function in the Pulse Generator in the Keysight Software Labber, by inputting the coefficients and timescales that describe the distortions. The predistorted signal will then correct for the over- and undershoots of the signal through the bias tee and, ideally, obtain the desired waveform. To get an intuition for the predistortion, the ideal signal is shown in Figure 22 (black). By deconvoluting this with $H(t)$, one gets the predistorted waveform that can now be used as input to correct pulse distortions described by the input parameters. Positive amplitudes correct for overshoots, so the input pulse is corrected to have a slower rise and thereby cancel out the overshoots, see the orange trace in Figure 22. Positive amplitudes are used for undershoots, and therefore brings the start of the input pulse to a larger amplitude.

2.3.1 Fitting and predistortion of bias tee pulse

Ideally, the timescales and amplitudes used for the predistortion can be established by fitting $H(t)$ to the bias tee signal. Since the timescales, and number thereof, are unknown, the initial guesses of the fit are best determined by visual inspection of the pulse, and the goodness of fit is then described by the reduced chi-square of the fit, which is defined by [15]:

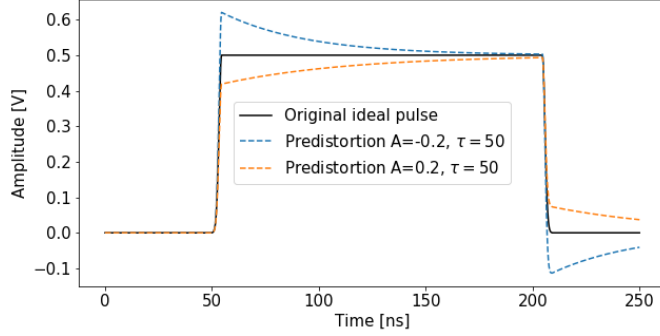$$\chi^2 = \sum_n \frac{(f(x) - y)^2}{\sigma^2}$$

Figure 22: An example of a predistorted waveform that can be used as input to a system to correct for distortions caused by it. As seen here, negative amplitudes correct for undershoots, and positive amplitudes correct for overshoots.

$$\chi^2_{reduced} = \frac{\chi^2}{N_{DOF}},$$

where N_{DOF} is the number of degrees of freedom which is defined as the number of points used for fitting minus the number of fit parameters. $f(x)$ and y are the values predicted by the fit function and the data points, respectively. σ is the uncertainty on the points, and this number is assumed to be the same for each point. The value of σ is established by the standard deviation of a measurement of 600 points of noise in the bias tee signal and, since the signal used for fitting is averaged 1000 times, dividing this value by $\sqrt{1000}$. For a good fit, the reduced χ^2-value should be equal to approximately 1. The fitting procedure is challenging, since there are many degrees of freedom involved. The first aspect to consider is selecting the region of the pulse to be fitted. For the bias tees used, the pulse fit region are chosen to span from where the pulse first reaches half of the pulse amplitude and 30 ns from this point, which is usually where the pulse has flattened out and reached its full amplitude. One exception to this is the QDev bias tee, where the amplitude decay happens on such a short timescale that the pulse amplitude is never at a steady value. Through simulated distortions of a perfect square pulse and of a pulse with a Gaussian rise of 3 ns, respectively, it was found that the parameters regarding the fitting region depends on the timescales themselves, and that a very good fit can be obtained (according to the reduced χ^2-value) without having found the correct timescales and amplitudes. However, since the pulse distortions are most prominent at approximately half the pulse amplitude, and this is where the fit regions are chosen to start.

An attempt at performing these fits is seen in Figure 23. The initial fit value for A_0 is set to 0.5 V, since the waveform rises up to approximately this amplitude, and the expression $1 + \sum_n A_n e^{-t/\tau_n}$ should therefore be scaled by this value. The rest of the

32

fit parameters are varied and tested, checking χ^2_{red} for each attempt and basing values on the previous fit (that is, the first two sets of initial fit values for the fit with three timescales is based on the fit result of the fit with two timescales, and so on). As can be seen in Figure 23, the reduced χ^2-value becomes smaller for each added timescale, as expected, since it should be possible to fit any waveform as long as there are enough fit parameters, but at some point this becomes overfitting. Note that, as the number of timescales (and amplitudes) becomes larger than 2, some of the fitted amplitudes become positive, indicating overshoots in the distorted waveform, which, from visual inspection of the pulse, does not seem to be accurate. Furthermore, the timescale of $\tau = 0.190$ ns in the fit with three timescale is very short and might not be physically realistic. In the fit with four timescales, there are two pairs of parameters where the timescales are almost equal (τ_1=0.392 ns and τ_3=0.361 ns), and the amplitudes are close to each other in value but with opposite signs ($A_1 = -3.00$ and $A_3 = 2.74$). These pairs of fit values that almost cancel each other out occur in fits for the other bias tees as well (see Appendix), and while they do not seem to have physical justification, they can be used to fit "bumps" in the waveform. While this is an effective way to get a better fit to the small ringing/irregularities in the pulse, it is not likely that these are actual physical parameters. These fit results are interpreted as a sign that the waveform is overfitted when the number of timescales becomes larger than two. However, since this fitting procedure is, as mentioned, dependent on the size of and location of fitting region and very sensitive to the initial fit parameters, an additional step is performed in order to increase the quality of the predistortion. A simulated predistortion is performed by deconvoluting the entire distorted output of the bias tee (not just a smaller region) with $H(t)$, and for the right parameters (i.e. the underlying distortion parameters), this should result in the ideal waveform. Here, the same cost function as before is evaluated to check how well the predistorted waveform matches the ideal waveform, that is, the integrated absolute difference between ideal and distorted pulse. Now, defining a function that takes in a number of amplitudes A and timescales τ, convolutes the distorted signal with $H(t)$ using these parameters, and returns the cost function value can be optimized to find the values of the $A's$ and $\tau's$ that minimize the cost function, using the input values as initial guesses. This is a more direct and faster way to find optimal predistortion parameters. This minimization method can then be used in combination with the fit results in order to improve the characterization method.

Like when fitting $H(t)$ directly to the distorted regions, this method depends highly on the initial parameters, but using the fit results as input should then be good starting points for the minimization process. The advantage of this additional step is that there are less degrees of freedom involved, since no specific regions of the data must be picked out for fitting.
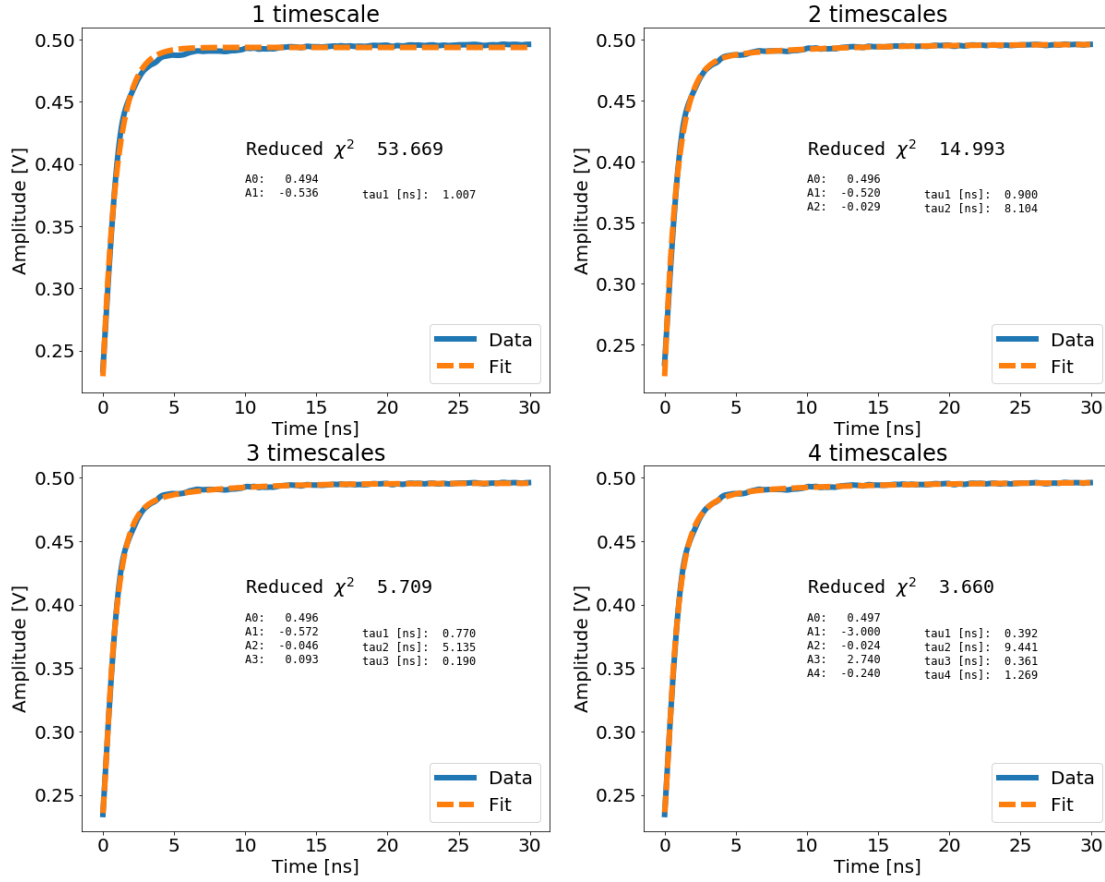
Figure 23: Fits with one to four timescales to the rise of the distorted output pulse from the Mini Circuits ZFBT-GW6+ bias tee.

As seen from the previous discussion, the amplitudes and timescales describing the distortions of the rise in the pulse can, although challenging, be found by fitting the waveform directly with the function $s_{out}(t) = A_0(1 + \sum_n A_n e^{-t/\tau_n})$. While for short pulses, this slow rise of the bias tee output signal is the main distortion, for longer pulses, a longer timescale is more prominent and has a larger contribution to the distortion of the pulse. This is the likely the amplitude decay discussed in section 2.2.1. The beginning of this amplitude decay can be seen in Figure 21, and increasing the plateau of the pulse, the full decay down to 0 V can be seen in Figure 24. This type of distortion is easily fitted with the function $f(t) = Ae^{-t/\tau}$, as can be seen in Figure 21 However, because of the absence of the term $+1$ in $f(t)$, this type of distortion cannot be corrected by use of $H(\omega)$. An attempt was made at predistorting the function by using and alternative $H'(\omega) = \sum_{n=1} \frac{iA_n\omega\tau_n}{i\omega\tau_n+1}$, that is, without the offset of 1. However, when deconvoluting the signal with this function, $H(\omega = 0) = 0$, which leads to division by zero. Setting
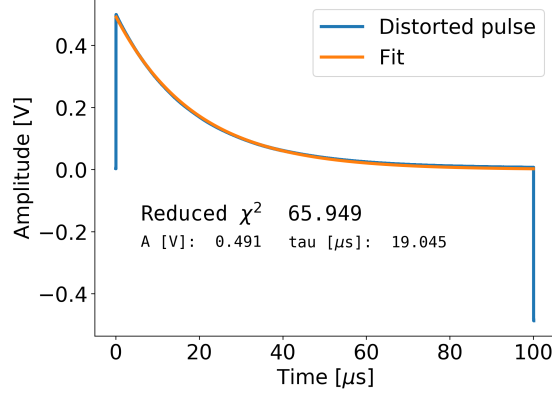
34

Figure 24: Fit of the form $f(t) = Ae^{-t/tau}$ to capture the decay of the pulse amplitude of the Mini Circuits ZFBT-6GW+ bias tee.

$H'(\omega = 0)$ equal to a value close to zero yielded the wanted shape of predistortion, but with a wrong scaling. Further attempts must be made in order to properly make up for this type of distortion, but due to limited time, this function was not properly implemented. However, it is effectively possible to correct this type of decay with time-scales that are not physical, but can be used to achieve approximately the correct shape for predistortion. This is done by combining two timescales, one long compared to the pulse plateau and with a negative amplitude, and another timescale which is smaller than the first, but still long compared to the pulse plateau and with a positive amplitude. Appropriate parameter values are found by using the minimization process described above. This approach is then used for predistorting the 500 ns bias tee output pulses from bias tees Mini Circuits ZFBT-6GW+, Mini Circuits ZFBT-4R2GW-FT and Anritsu SC17771. However, this way of predistorting the long timescales becomes less accurate for very long plateaus where the exponential nature of the decay becomes more prominent. It is easier to correct the decay when only the relatively flat part of it is present, like in the case of the 500 ns pulses used. Since the amplitude decay of the QDev bias tee happens on a very short timescale ($\sim$ 110 ns), the amplitude drops all the way down to zero during the 500 ns, and so the full exponential decay is present in the waveform. Additionally, predistorting this entire decay would require a waveform with amplitudes outside the range allowed by the AWG. Therefore, the pulse used for the QDev bias has a plateau of only 100 ns in order to be able to predistort it.

To sum up the approach for each bias tee: the long timescales and corresponding timescales are found by using the minimization process to find two sets of parameters that effectively predistort the waveform. Then, the fit results of the short timescale fits are investigated by testing out the sets of parameters by simulated predistortion with

them. Again, simulated predistortion refers to deconvoluting the bias tee signal with $H(t)$. Investigating how much the simulated predistortion improves with each added timescale and combining this with considerations about the χ^2_{red}-value of each fit and the probability that the fitted parameters are physically accurate, one of the fit results is chosen as the starting point. Then, the chosen fit result and optimized parameters for the long-timescale distortion are combined, and possibly another minimization is performed with all these parameters passed as inputs at the same time. In some cases, the fit parameter results are slightly varied by hand before passing them to the minimizer, in order to find any nearby minima of the cost function. For the Mini Circuits ZFBT-6GW+ bias tee, for example, the two timescales fit result is used, since the simulated predistortion yields similar results for the 4 different sets of fit parameter results, and all amplitudes in this fit result are negative, which is likely the most accurate description. For the remaining bias tees, the number of timescales used can be seen in Table 1, along with the cost function values for each predistortion result. The cost function values are normalized by diving by the amount of points in the waveform, since the datasets for the QDev bias tee and the other bias tees are not of equal length. The actual long timescales and amplitudes describing the amplitude decays of the pulses are shown in Table 2.

The final parameters are now used to generate the predistorted signal via the AWG, and the bias tee outputs are seen in Figures 25, 26, 27 and 28. The right plots of these figures show the difference between ideal trace and predistorted bias tee trace, respectively. For perfect predistortion, there is no difference in between the ideal trace and the bias tee trace, and so, the better the predistortion, the more the deviation versus time looks like a straight horizontal line at zero voltage.
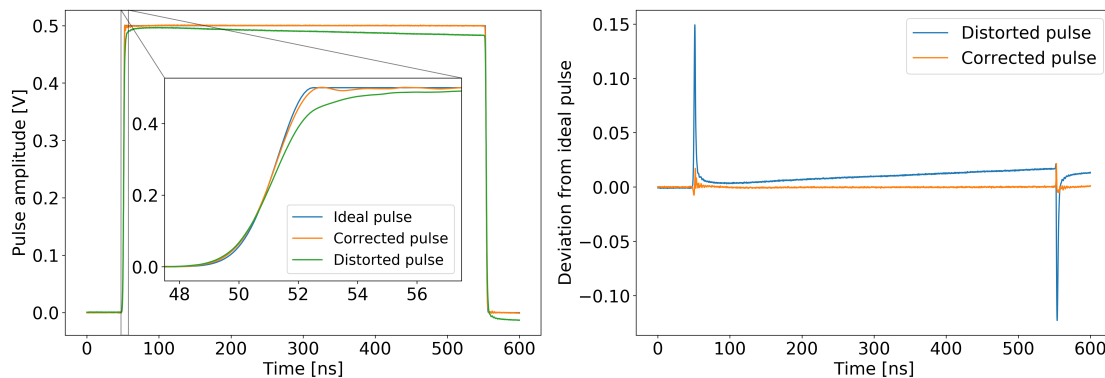

Figure 25: Mini Circuits ZFBT-6GW+ bias tee. Left: Original distorted pulse along with predistorted and ideal pulse. Right: the difference between the ideal pulse and the distorted and corrected pulse as a function of time.

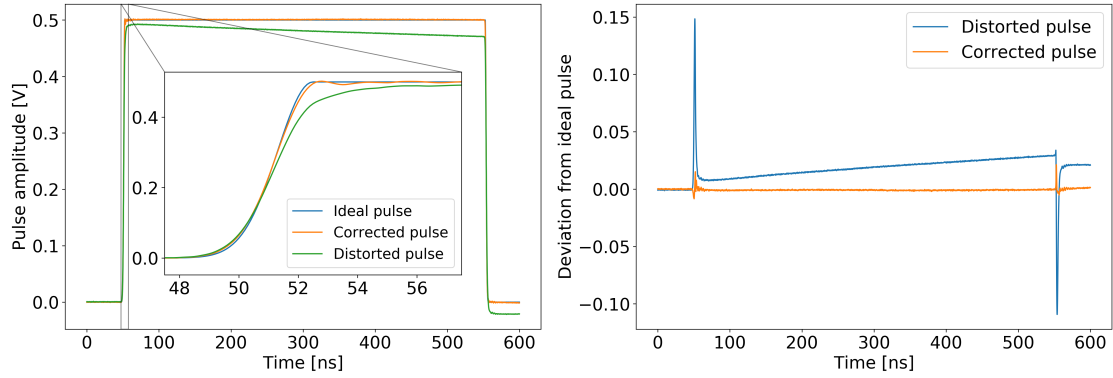As can be seen from these figures, perfect predistortion is not obtained, mainly due

36

Figure 26: Mini Circuits ZFBT-4R2GW-FT bias tee. Left: Original distorted pulse along with predistorted and ideal pulse. Right: the difference between the ideal pulse and the distorted and corrected pulse as a function of time.
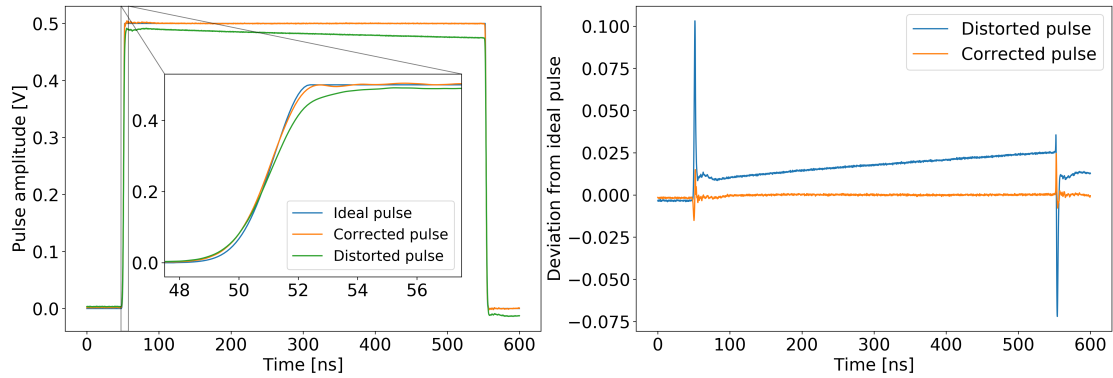

Figure 27: Anritsu bias tee. Left: Original distorted pulse along with predistorted and ideal pulse. Right: the difference between the ideal pulse and the distorted and corrected pulse as a function of time.

to some ringing and noise in the signal that cannot be removed by predistortion. Additionally, it is possible that the timescales and coefficients found do not describe the distortions perfectly, since the minimizer for the simulated predistortion is very sensitive to the input initial guesses. However, these were the best results obtained by varying the initial guesses and investigating the resulting integrated absolute difference between ideal and bias tee pulse. As seen from Table 1 and Figure 28, the QDev bias tee yielded the most distorted signal, and also the worst result after predistortion. This is, as mentioned, due to the much shorter timescale of the amplitude decay, making the waveform harder to correct with amplitudes and time-scales that are not based on actual physical parameters

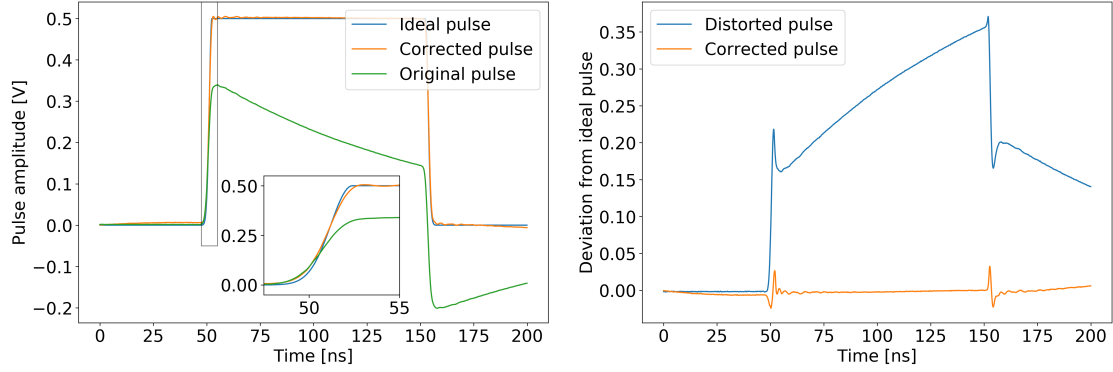For the QDev bias tee, the Mini Circuits ZFBT-4R2GW-FT and the Anritsu bias tee,

Figure 28: QDev bias tee. Left: Original distorted pulse along with predistorted and ideal pulse. Right: the difference between the ideal pulse and the distorted and corrected pulse as a function of time.

the fits to the rise of the pulses as well as the amplitude decay fits can be seen in the Appendix.

Bias tee	Deviation before [$\times 10^{-3}$ V·ns]	Deviation after[$\times 10^{-3}$ V·ns]	Coefficients [V]	Timescales [ns]
Mini Circuits ZFBT-6GW+	9.570	0.452	-0.52012	0.899563
			-0.0289279	8.10373
			-0.448667	3146.55
			0.444304	2101.89
Mini Circuits ZFBT-4R2GW-FT	17.569	0.904	-0.532695	0.905352
			-0.0113658	5.49531
			-0.459165	3156.02
			0.445789	1734.58
Anritsu SC7771	16.174	0.591	-0.482383	0.825
			-0.419285	2914.94
			0.401536	1787.83
			-0.565678	7.69601
			0.578098	7.23486
QDev bias tee	178.717	3.311	-0.515519	0.700
			-1.1422	1315.37
			0.872921	119.922
			-0.0136605	-30.7826
			-0.0276486	4.86977

Table 1: For each of the four bias tees, the integrated absolute difference (Deviation) per point between the ideal pulse and distorted pulse as well the corrected pulse is listed. Additionally, the coefficients and timescales used for the predistortion are listed.

3 Cryoscope Simulation

As mentioned, the purpose of the cryoscope method is to reconstruct a pulse from its effect on the qubit, and thereby being able to characterize the distortions that the pulse has been subjected to from elements inside the cryostat. To try out this method, a

Bias tee	Coefficients [mV]	Timescales [μs]
Mini Circuits ZFBT-6GW+	0.491	19.045
Mini Circuits ZFBT-4R2GW-FT]	0.485	19.726
Anritsu SC7771	0.474	20.456
QDev bias tee	0.342	0.110773

Table 2: The fit parameters for each of the four bias tees when fitting $f(t) = Ae^{t/\tau}$ to a pulse where the full amplitude decay is visible.

simulation is done in order to inspect involved parameters, and to generally prepare for performing the actual experiment to see which considerations are important. The simulation is done using the Lindblad master equation solver (mesolve), in the software QuTiP (Quantum Toolbox in Python) [18]. This is done by using the two-level approximation of the Hamiltonian of the flux-tunable transmon (Equation 6) in a frame rotating at the sweet spot qubit frequency, $f_{01}(\Phi_{ext} = 0)$. As derived, this Hamiltonian depends on the external magnetic flux through the circuit loop, resulting in a time-dependent Hamiltonian for a time dependent Φ_{ext}. Using the ideal and distorted pulses, respectively, from the simple room temperature bias tee setup (for bias tee Mini Circuits ZFBT-6GW+), the dynamics of a single flux-tunable transmon subjected to a flux pulse can be simulated this way. Additionally, T_1 and T_2 decay can be implemented in the simulation by including the collapse operators $\sqrt{\frac{1}{2T_2}}\sigma_z$ (dephasing) and $\sqrt{\frac{1}{T_1}}\hat{a}$ (decoherence) in the mesolve function. In this simulation, the timescales for decoherence are set to $T_1 = 10\mu s$ and $T_2 = 1\mu s$. Since $V = IR = \frac{\Phi_{ext}}{M}R$, i.e. $V \propto \Phi_{ext}$, voltage to flux conversion is simpy perfomed by directly scaling the pulse amplitude to yield the wanted flux pulse amplitude. As an example, a flux pulse of amplitude $\Phi_{ext} = 0.25\Phi_0$ is studied, resulting in a detuning of $\Delta f = 1$ GHz for parameters $E_C/h = 0.25$ GHz and $E_J/h = 19.5$ GHz. The excursion to this detuning is visualized in Figure 29(a), and the pulses in units frequency used to implement this detuning are shown in Figure 29(b). Including simulations of the first and last $\pi/2$-pulses, plotting the trace of $\langle\sigma_x\rangle$ throughout the experiment yields the plot in Figure 31(a). As can be seen, the expectation value of σ_x, or the X component on the Bloch sphere, starts at 0 at time $t = 0$, because the qubit is prepared in $|0\rangle$ at the top of the Bloch sphere. Applying the $\pi/2$ pulse causes the qubit to go to the $|+\rangle$ state which is on the equator of the Bloch sphere, yielding $\langle\sigma_x\rangle = 1$. Since the Hamiltonian is in a rotating frame, $\langle\sigma_x\rangle$ now oscillates at a frequency
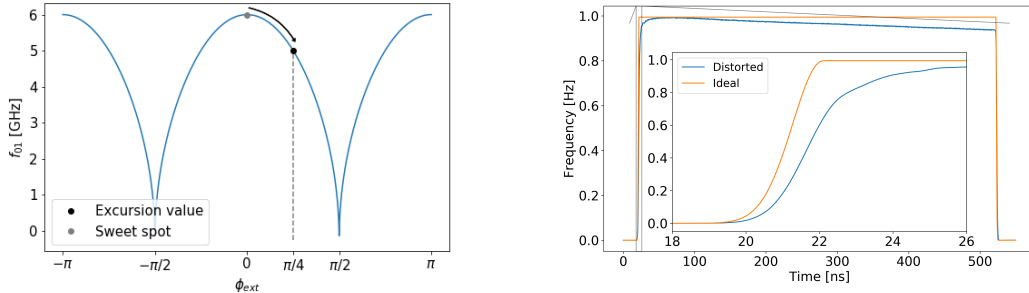
(a) The energy of a flux-tunable transmon as a function of external flux. The excursion to $\phi_{ext} = \frac{\pi}{4}$ detunes the qubit 1 GHz from the sweet spot.

(b) A trace of the input pulses (ideal and distorted) in terms of frequency (detuning).

Figure 29

$\Delta f = f_q(0) - f_q(\Phi_{ext})$. The time resolution of this trace acquired from the simulation is limited by the sampling rate of the AWG. In the simulation, one has knowledge of the qubit state at each point in time, and so the data necessary for the reconstruction process can be obtained by inspecting one long flux pulse. If actually executing the experiment, each of the data points in the $\langle \sigma_x \rangle$ trace would correspond to the result of one full experiment.

Fourier transforming the pulses yields the spectra, which can be seen in figure 32. Here, it is clear that the ideal pulse has one well-defined peak at the detuning frequency, because the pulse stays at this amplitude for the majority of the pulse, and is only widened by the smaller frequencies that the pulse amplitude has to traverse on the way to its full amplitude during the Gaussian rise. The spectrum of the distorted pulse demonstrates how the much slower rise of the pulse along with the amplitude decay leads to the signal only being at the full amplitude for a very small part of the pulse. This means that the spectrum is broadened very much compared to the spectrum of the ideal pulse. Now, the goal is to reconstruct the waveforms from the trace of $\langle \sigma_x \rangle$. This is done with an alternative approach compared to the one used by Rol et al. Instead of measuring both $\langle \sigma_x \rangle$ and $\langle \sigma_y \rangle$ for each point in time, determining the corresponding phases at the beginning and end of a small time window Δtau, and from there estimating the average detuning in this time window, a simpler approach is taken. Here, only the $\langle \sigma_x \rangle$ trace is used, meaning that only $\langle \sigma_x \rangle$ data is needed for each point in time. The frequency of the oscillations are then analysed directly to reconstruct the waveform.

This is done by dividing the oscillating region of the trace into small time windows of duration Δt and fitting the data in each of these windows with a function $f(t) = A\cos(2\pi f t - \phi)$. Here, A is the amplitude of the oscillations in the given time window, f
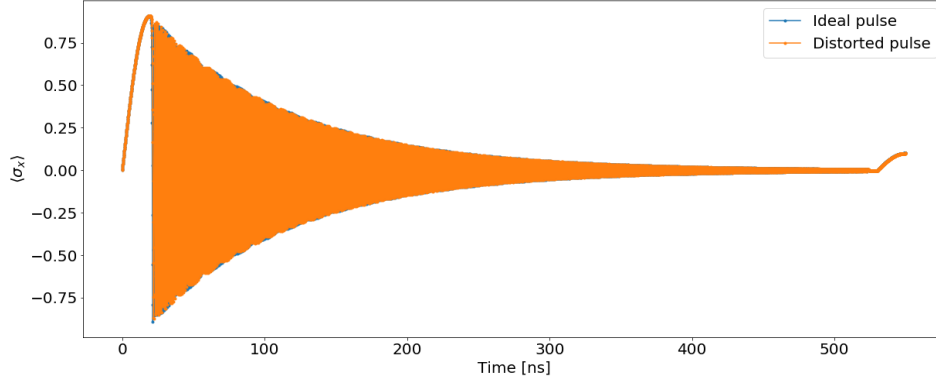
40

Figure 30: Trace of $\langle \sigma_x \rangle$ for T_2=100 ns. Here, it can be seen how the short T_2 limits the length of the timescales to be resolved when investigating pulse distortions.

is the frequency, and ϕ is some phase offset. From each time window, the fitted frequency is then extracted, and this can now be used to map the frequency of the oscillations to the amplitude of the flux pulse, thereby reconstructing the shape of the signal. The distortions of the pulse can then be observed, fitted and ultimately corrected.

It is worth noting the importance of a large T_2 for this method. In Figure 30, the $\langle \sigma_x \rangle$ trace is shown for a short T_2 of 100 ns. Due to dephasing of the qubit, the oscillations die out while the flux pulse is applied, and thus, no frequencies can be extracted for pulse reconstruction. This poses a limitation for the duration of the pulse, and thereby a limitation of the distortion timescales that can be resolved. Therefore, a long T_2 (compared to pulse plateau length) is essential for the success of the cryoscope method.

In the process of fitting $f(t)$ to the data in the time windows, several degrees of freedom in this procedure must be taken into account. First of all, the fits are generally very sensitive to initial fit parameters, and so these must be set to appropriate values in order to consistently get fits of good quality. For each window, the initial amplitude guess is set to the largest absolute value in the window, i.e., $A_{initial} = \langle \sigma_x \rangle_{max}$, and the frequency guess is $f_{initial} = \frac{1}{2\bar{T}}$, where $\bar{T}$ is the average time between maxima and minima in the time window. The initial phase guess is $\phi_i = 2\pi f_{initial} t_{max}$, where t_{max} is the time in the time window at which the maximum $\langle \sigma_x \rangle$ occurs. For these initial parameters to best represent the data, each time window should be large enough to contain enough full oscillations to accurately fit the frequency. However, since during the rise and fall of the pulse, the frequency changes very fast (approximately 4.5 ns from 0 to full amplitude), in order to attribute a single frequency to one time window, the time window size should be small such that not too many different frequency values are present in one window.
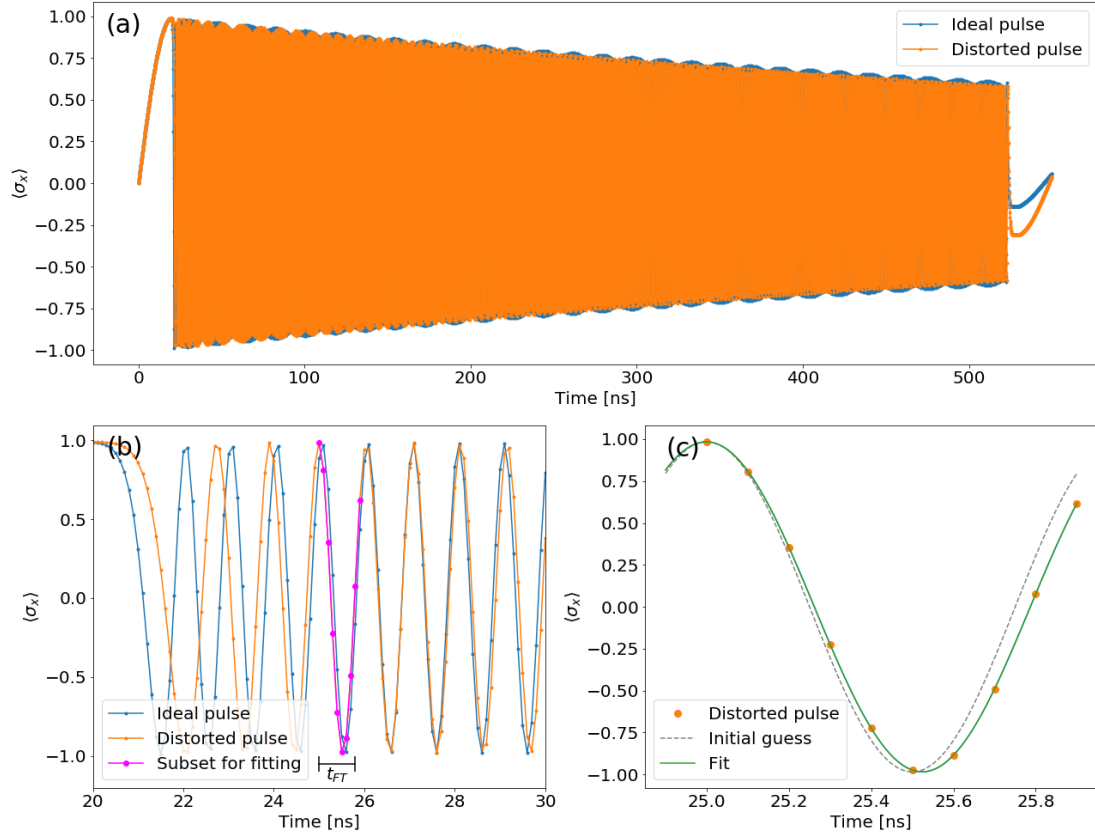
41

Figure 31: (a): $\langle\sigma_x\rangle$ plotted as a function of time throughout the simulated experiment. Since the simulation is performed rotating frame (rotating at the sweet spot frequency), $\langle\sigma_x\rangle$ oscillates with the detuning from the sweet spot frequency. The amplitude of $\langle\sigma_x\rangle$ decays eponentially on a time scale T_2. The detuning here is $\Delta_f = 1$ GHz. (b): A zoom-in of the $\langle\sigma_x\rangle$ trace, showing the oscillations more clearly. Here, a small time window of size Δt is isolated and analyzed in (c), where a function of form $f(t) = A\cos(2\pi f t - \phi)$ is fitted to the data. The function is plotted for the initial fit parameters (grey) and for the actual fit (green). In this example, $\Delta t = 1$ ns

Furthermore, the larger flux pulse amplitude, and thereby detuning frequency, the faster oscillations in the rotating frame. This in principle means that the time windows can be smaller, such that shorter timescales can be resolved - however, since the temporal resolution is fixed and limited by the AWG, this limits the number of points per oscillation, which can cause aliasing and thereby reduce the quality of the fits. These considerations about time window size versus pulse amplitude can be investigated by plotting the cost function (the area between reconstructed and actual waveform) as a function of time window size for various pulse amplitude. This procedure should help find an optimal
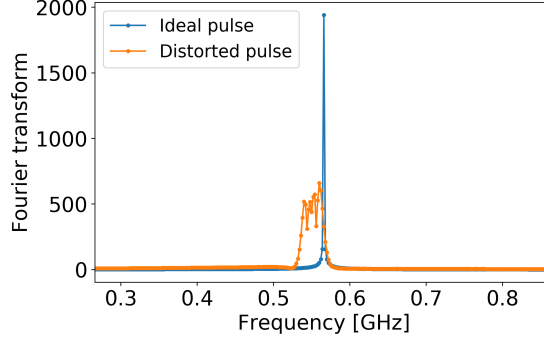
Figure 32: Spectrum of the oscillating region of the $\langle \sigma_x \rangle$ trance seen in Figure 31(a), for the distorted as well as the ideal pulse

combination of parameters and is done later in this section.

As a starting point, the fitting of each time window is unbounded. However, outliers in the reconstructed pulse can occur, typically in the form of fitted frequencies that are higher than the actual frequencies. This is circumvented by adding the constraint that each frequency must be within a certain value range from the previously fitted point. This value range is decided from the maximum difference in frequency between consecutive points in the ideal pulse and is set to $0.08\Delta_f$, where Δf is the wanted frequency detuning. This constraint is implemented in the fitting process of $\langle \sigma_x \rangle$ for both the distorted and ideal pulse such that the fits are unbounded unless the requirement about consecutive points is not fulfilled, in which case a new, bounded fit is performed. In this case, the initial frequency $f_{initial}$ is now the frequency of the previously fitted point. This conditional way of implementing the bounds is to improve computational speed. It should be noted that the value $0.08f_{max}$ established from the ideal pulse is only a "good" constraint when the distorted pulse rises more slowly than the ideal pulse, since in that case, the distance in terms of frequency between consecutive points must be smaller in the distorted pulse than in the ideal pulse. This conditional bounding of the fits can however cause the fit values to get trapped in a certain frequency range, yielding a poor reconstruction. This is only a problem for larger time window at larger frequency detunings, however. As a solution to this, an additional requirement for the reduced χ^2-value of the previous fit is set for time window sizes above 1.2 ns. This means that consecutive points must only be within $0.8\Delta f$ of each other if the previous fit was actually good.

The fall of the pulse is not included in the reconstruction, since equivalently to the rise of the pulse, the fast changes in frequency give rise to fitting challenges, and this part of the pulse is not necessary for the fitting and minimization procedure when characterizing the predistortion parameters. Since the pulse parameters for predistortion can be found
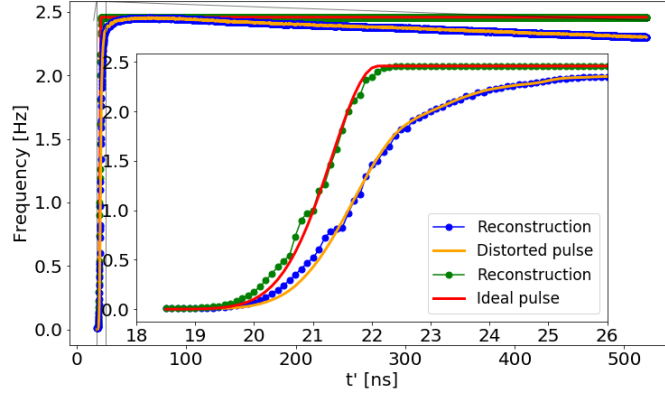
43

Figure 33: Original ideal and distorted pulse in units of frequency, along with the reconstructed pulses obtained via the cryoscope method for detuning $\Delta f = 1$ GHz from the sweet spot and a time window size of 1 ns.

without this region present, it is therefore left out such that that poor reconstruction here does not contribute to the overall cost function value.

The reconstructed pulse for an excursion to $\phi_e = 0.25\pi$ using 1 ns time windows is seen in figure 33. Each point is plotted versus t', which is defined as the middle time point in the time window, i.e. $\Delta t/2$. In order to compare the reconstructed pulses with the actual pulses, the latter must be shifted forward in time by $\Delta t/2$. In general, the the whole reconstructed pulse follows the actual pulse shape well, especially in the long middle region, where changes in frequency are slow in the case of the distorted pulse. Qualitatively, it can be seen in the zoom-in how the pulse rise is not completely smooth, due to fitting problems related to the fast changes in frequency, as discussed above. Quantitatively, the quality of the reconstruction is assessed by consulting a similar cost function to the one used for assessing predistorted pulses. This cost function is the integrated absolute difference between reconstructed and actual pulse, normalized by dividing by number of points and pulse amplitude in terms of frequency.

In order to find out whether there is an optimal size for the time windows for reconstructing a pulse of a certain/given amplitude, the integrated absolute difference (deviation) between reconstructed and actual point is found for a sweep over time window size from 0.4 ns to 2 ns for pulse amplitudes in terms of frequency from 0.5 GHz to 2.5 GHz, see Figure 34. The blue curves show the deviation per point for the entire reconstructed pulse. However, since the kinks in the reconstruction are most prominent in the rise of

44

the pulse, the deviation is also inspected just for the first 5 ns of the pulse, i.e. the rise of the pulse. As can be seen by the vertical scales of each measure/graph, the deviation per point is higher for the pulse rise only compared to the deviation per point for the entire pulse, confirming that the pulse rise is the most "problematic" region of the pulse, i.e., hardest to fit/reconstruct accurately. Neither of these graphs show a clear pattern of a an optimal window size, but there are minima to be inspected. Since the minima of the pulse deviations occur at different time window sizes for the rise and the entire pulse, respectively, one can asses the reconstruction quality by inspecting the shape at each optimal window size and inspect if the timescales that were previously found can be found again by fitting. The plots discussed are not very smooth, almost shows oscillatory behaviour. This is most likely a reflection of the jumps that occur in especially the rise of the reconstructed pulse, giving rise to very non-smooth/non-continuous waveforms. The reason for these kinks in the waveforms is not completely certain, but could maybe be attributed to the way that a point in time is mapped to a certain frequency. While the fitted frequency of each time window has been associated with the middle point of each time window, this might not be the optimal mapping, and furthermore, the "optimal mapping" might change along the waveform. For $\Delta f = 1$ Ghz, the optimal window sizes for reconstructing the distorted pulse are 0.4 ns and 1.1 ns for the full pulse and the pulse rise, respectively, see Figure 34. The reconstructed pulses can be seen in Figure 35. For the optimal window size decided by the full pulse (Figure 35(a)), a sudden jump occurs at approximately half the full amplitude of the reconstructed pulse, and more similar, but smaller, jumps occur at larger t'. The optimal window size decided by only the pulse rise shows deviations as well, but these are smaller and smoother. Now, the region of each of the two pulses from half the pulse amplitude and 30 ns forward is picked out, and is fitted for two timescales (since two timescales were deemed the best fit for the Minin Circuits ZFBT-6GW+ bias tee, see section 2.3.1). The error of each data point is now defined as the standard deviation obtained from the covariance matrix of the frequency fitting process, and corresponding error bars are shown in 36. The inital fit parameters passed to each of the fits are the fit results from the previous fitting. The result in Figure 36 shows that approximately similar timescales as for the fit to the actual pulse are found (A_0 should not be compared, since the pulses are in different units and therefore have numerically different amplitudes). The amplitude of the ~ 0.8 ns timescale is somewhat larger for the fit in Figure 36(b) compared to the original fit (-0.795 versus -0.520), and the reduced χ_2-value indicates a significantly worse fit, compared to the original fit as well as that in Figure 36(a). This confirms that for $\Delta f = 1$ Ghz, the optimal window size for fitting the pulse rise is 1.1 ns.

Running the minimization of the long timescales of the 0.4 ns time window pulse yields parameters $A_3 = -0.4509$, $\tau_3 = 4329.63$ ns and $A_4 = 0.4555$, $\tau_4 = 1806.35$ ns. For
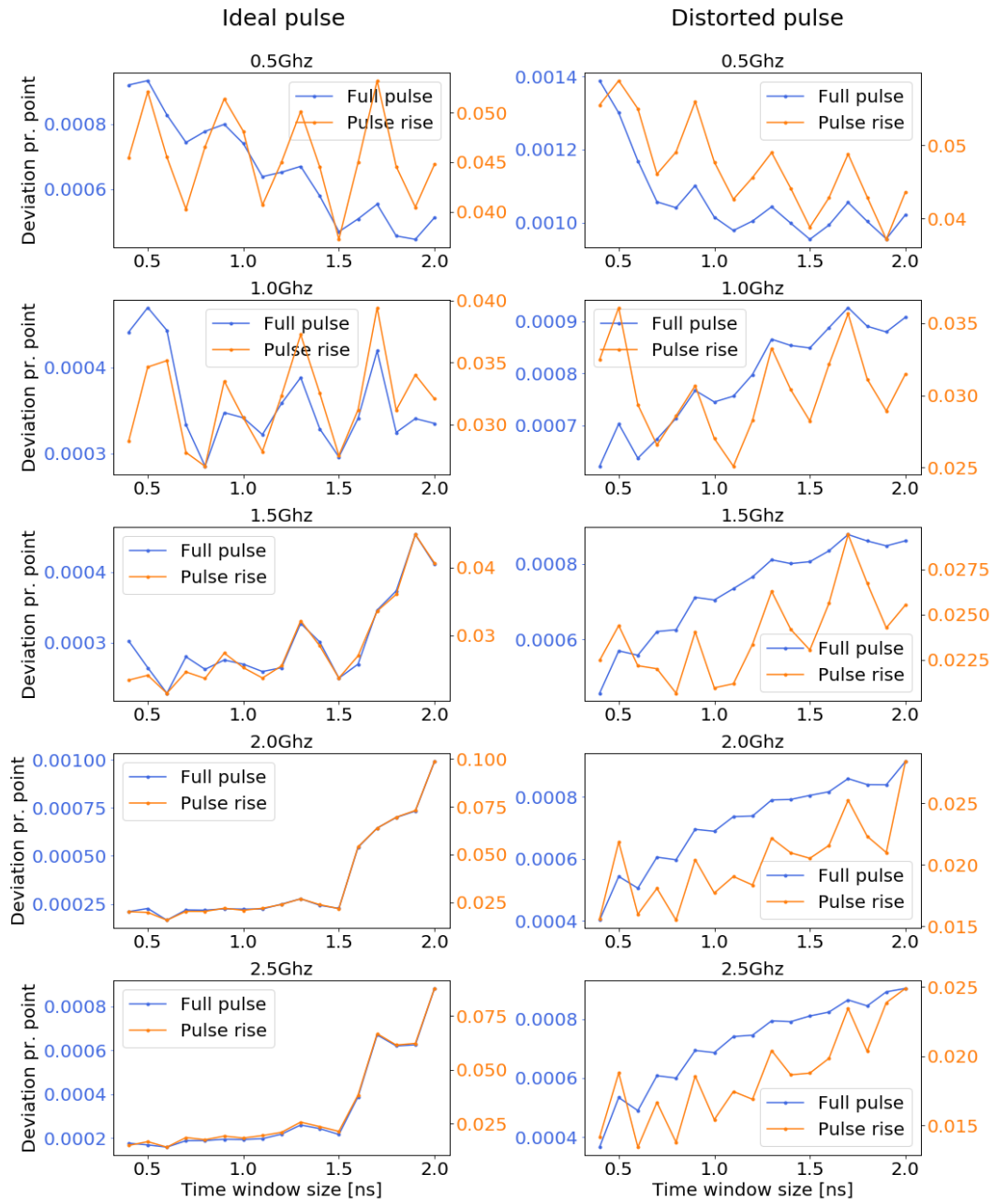
45

Figure 34: Deviation of the reconstructed waveform as a function of Δt for five different detunings (0.5 GHz - 2.5 GHz.)

1.1 ns time window, $A_3 = -0.4506$, $\tau_3 = 4332.37$ ns, $A_4 = 0.4553$, $\tau_4 = 1804.02$ ns. These parameters are very similar, which might suggests that the pulse region where the amplitude decay happens is not as sensitive to the choice of window size. When deciding the window size for a given detuning, the deviation of the reconstructed pulse rise from the actual pulse should be given the most thought. Referring to the deviations of the pulse rise in the right panel of Figure 34, it is not straightforward to generalize the optimal time window size, but as a rough estimate, the optimal time window size could be said to be $\Delta t = \frac{1}{\Delta f}$.
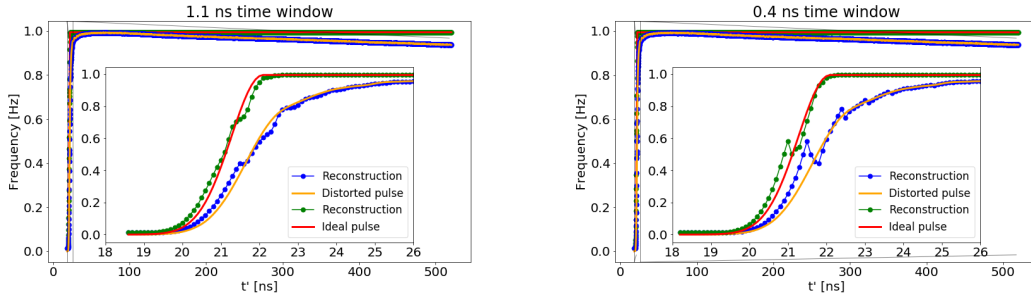
(a) Ideal and distorted waveform reconstructed via cryoscope with Δf=1 GHz and Δt=1.1 ns.

(b) Ideal and distorted waveform reconstructed via cryoscope with Δf=1 GHz and Δt=1.1 ns.
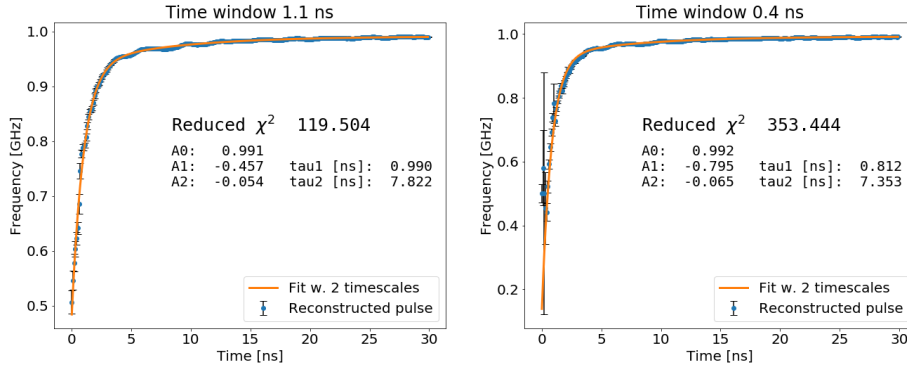
Figure 35

Figure 36: Fitting the rise of reconstructed waveform for a cryoscope simulation performed at detuning $\Delta f = 1$ GHz for window sizes of 1.1 ns (left) and 0.4 ns (right).

47

3.1 Verification of cryoscope

As a way of verifying the correction of a distorted pulse, a sweep of flux pulse amplitudes can be applied to the two-qubit system in state $|10\rangle$ to produce a Chevron pattern as seen in Figure 7(b). When the flux pulse amplitude is $\Phi_{ext} = \Phi_{iSWAP}$, this constitutes an iSWAP gate (for appropriate pulse duration). To visualize this, a simulation of this experiment is performed. This simulation assumes a system of two coupled flux-tunable transmons and, as described in section 1.2 the Hamiltonian for this system is:

$$H = (E_0 |0\rangle \langle 0| + E_1 |1\rangle \langle 1|) \otimes \mathbb{1} + \mathbb{1} \otimes (E_0 |0\rangle \langle 0| + E_1 |1\rangle \langle 1|) + \frac{g}{2}(\sigma_x \otimes \sigma_x + \sigma_y \otimes \sigma_y)$$

$$= \begin{pmatrix} E_{00} & 0 & 0 & 0 \\ 0 & E_{01} & g & 0 \\ 0 & g & E_{10} & 0 \\ 0 & 0 & 0 & E_{11} \end{pmatrix}$$

This is a subspace of the Hamiltonian in equation 12, containing only the actual qubit states in the computational space. Preparing the system in $|10\rangle$ (can be done by applying a $Y_{\pi/2}$ pulse to $|00\rangle$ like in the cryoscope experiment), and the flux pulse is applied by simulating the system evolution due to the H when varying flux on qubit 1. If no distortions are present, running this for an array of flux values yields a chevron pattern as seen in Figure 7(b), as soon as the pulse has reached its full amplitude. Now, running this simulation with distorted and predistorted flux pulses (scaled signal outputs from the Mini Circuits ZFBT-6GW+ bias tee) yields the patterns in Figure 37(a) and (b), respectively. Here, the distortion of the chevron pattern due to especially the long timescales can be clearly observed in Figure 37(a), and the predistorted waveform yields a corrected pattern, confirming the effect of the predistortion.
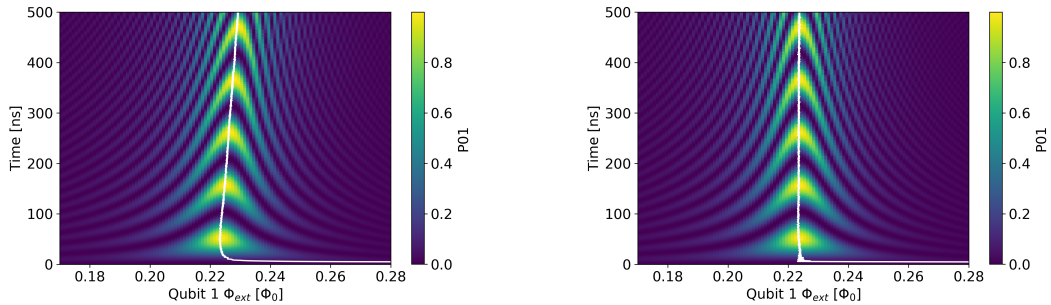
(a) Population of $|01\rangle$ as as a function of time and magnetic flux of qubit 1. The distortions of the waveform used to simulate the flux pulse are clearly seen. The white curve indicates the flux pulse shape for $\Phi = \Phi_{i\text{SWAP}}$.

(b) The chevron experiment performed with the corrected waveforms.

Figure 37

4 Conclusion and outlook

Several aspects of pulse distortions have now been investigated. In section 2, the predistortion of the output waveforms of four different bias tees yielded deviations down to $4.52 \cdot 10^{-4}$ V·ns per point. It was found that trying to determine the characteristic parameters of the distortions even in a simple setup is a challenging task. Fitting the theoretical step function $s_{out}(t) = A_0(1 + \sum_n A_n e^{-t/\tau_n})$ directly to the distorted pulses did return some likely parameters that could be used for pulse correction. However, the pulse corrections could still be improved, and this is likely due to the problem of selecting a region of the pulse to be fitted, along with good initial fit parameters. These many degrees of freedom result in a very time-consuming process. The implementation of the minimization of the deviation of pulses is a potential way of making the characterization process more efficient. It can both be used as an extra step to increase the quality of the correction performed with the parameters extracted from the fit to the pulse rise, but also as a way of predistorting a pulse even without physically realistic parameters. The minimization process can then be used to find parameters that effectively predistort pulses, even though they are not rooted in actual physical timescales. The downside of this is that the minimization process would have to be redone for every different plateau or width. If the underlying distortion parameters were found, one should be able to predistort all pulse shapes with the same parameters and obtain the (approximately) ideal waveform. Furthermore, as discussed, the amplitude decays observed in the distorted pulses are difficult to correct when using the method of effectively predis-

49

tort with parameters that are not physically likely. An obvious next step for improving the pulse correction is then to implement a way to deconvolute distortions of the form $f(t) = Ae^{-t/\tau}$.

In section 3, the effects of these pulse distortions on a qubit were investigated by simulating the cryoscope experiment and analyzing the frequency of the qubit precession around the z-axis of the Bloch sphere in a rotating frame. The reconstruction of the pulses was executed in a slightly different way from the method used by Rol et al.[1], and this approach used relies on many parameters such as initial fit values and optimal time window size given a certain detuning from the sweet spot. It was found that reconstructing the rise of the pulses was the most challenging part, while the flatter regions of the pulses were reconstructed well in comparison. Even though this was a simpler, or at least less careful approach than the full procedure described in Rol et al., reconstructions of the pulses were still made, such that fitting to the rise of the reconstructed pulse yielded approximately the same parameters as for the actual pulse. This suggests that the cryoscope is a robust method of reconstructing pulses, at least when simulating the procedure. The next natural step would be to test the method on an actual qubit and possibly do a comparison of this simpler approach to the more sophisticated one of Rol et al in order to further explore advantages and disadvantages of the two methods.

References

[1] Rol et al. (2020). *Time-domain characterization and correction of on-chip distortion of control pulses in a quantum processor.* Appl. Phys. Lett. 116, 054001

[2] D.T. Sank (2014). *Fast, Accurate State Measurement in Superconducting Qubits.* Phd thesis, University of California Santa Barbara

[3] Krantz et al. (2019). *A Quantum Engineer's Guide to Superconducting Qubits* Applied Physics Reviews. 6. 021318. 10.1063/1.5089550.

[4] D.P. Divincenzio (2000). The Physical Implementation of Quantum Computation. Fortschritte der Physik 48(9-11)

[5] N. K. Langford (2013). *Circuit QED — Lecture Notes.* arXiv:1310.1897 [quant-ph]

[6] Koch et al. (2007). Charge insensitive qubit design derived from the Cooper pair box. Physical Review A. 76. 10.1103/PhysRevA.76.042319.

[7] M.D. Reed (2013). *Entanglement and Quantum Error Correction with Superconducting Qubits.* Phd thesis, Yale University

[8] DiCarlo et al. (2009). *Demonstration of two-qubit algorithms with a superconducting quantum processor.* Nature 460, 240–244 (2009). https://doi.org/10.1038/nature08121

[9] Z. Chen (2018). *Metrology of Quantum Control and Measurement in Superconducting Qubits.* Phd thesis, University of California Santa Barbara

[10] Steven W. Smith (1997). *The Scientist and Engineer's Guide to Digital Signal Processing.* California Technical Publishing.

[11] K. F. Riley & M. P. Hobson (2011). *Essential Mathematical Methods for the Physical Sciences.* Cambridge University Press

[12] Robert J Marks II (1991).*Introduction to Shannon Sampling and interpolation theory.* Springer-Verlag New York.

[13] J. R. Andrews (2008). *Broadband Coaxial Bias Tees (Application Note AN-1f).* Retrieved July 15, 2021 from `https://www.yumpu.com/en/document/read/10972826/an-1f-broadband-coaxial-bias-tees-picosecond-pulse-labs`.

[14] Lee Teschler (2015). *When inductors self resonate.* Retrieved June 11, 2021 from `https://www.analogictips.com/when-inductors-self-resonate/`

[15] R.J. Barlow (1989). *Statistics - A Guide to the Use of Statistical Methods in the Physical Sciences*. John Wiley And Sons Ltd.

[16] Datasheet for Mini Circuits ZFBT-6GW+. Retrieved from `https://www.minicircuits.com/pdfs/ZFBT-6GW+.pdf` May 7, 2021.

[17] J.D Irwin & R.M. Nelms (2015). *Basic Engineering Circuit Analysis* (11th edition). Wiley.

[18] *Quantum Toolbox in Python:* `https://qutip.org/`

[19] *Passive High Pass Filter*. Retrieved January 15, 2022 from `https://www.electronics-tutorials.ws/filter/filter_3.html`

[20] *RC step response*. Retrieved January 15, 2022 from `https://spinningnumbers.org/a/rc-step-response.html`

[21] J. Butscher (2018).*Shaping of Fast Flux Pulses for Two-Qubit Gates* [Master's thesis]. Quantum Device Lab ETH Zürich.

[22] B. Li. *Pulse-level circuit simulation with QuTiP*. Retrieved from `https://nbviewer.ipython.org/github/qutip/qutip-notebooks/blob/master/examples/qip-noisy-device-simulator.ipynb`) September 3, 2021.

Appendix

(a) Ideal and distorted ouput pulse from the Mini Circuits ZFBT-4R2GW-FT bias tee. The short-timescale fit region is indicated as well.

(b) Fit of the form $f(t) = Ae^{-t/tau}$ to capture the decay of the pulse amplitude of the Mini Circuits ZFBT-4R2GW-FT bias tee
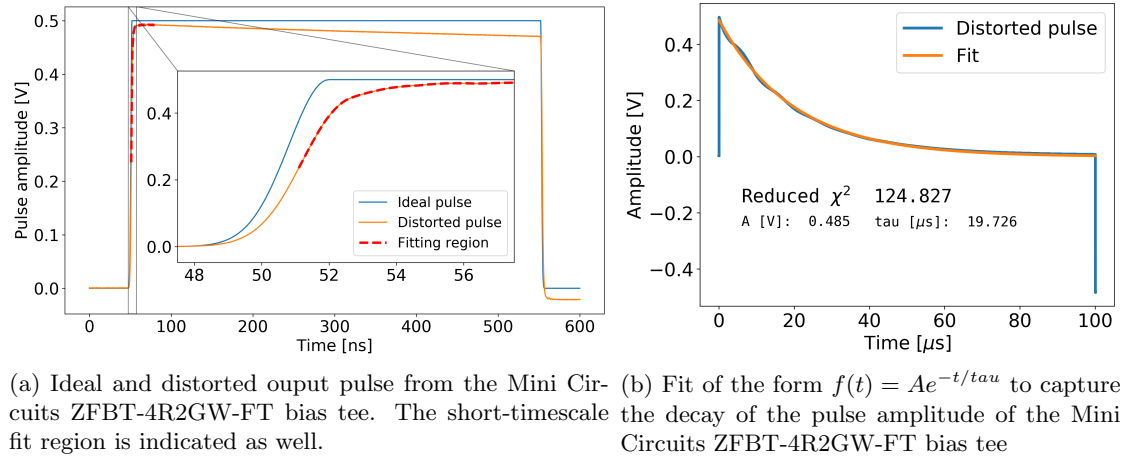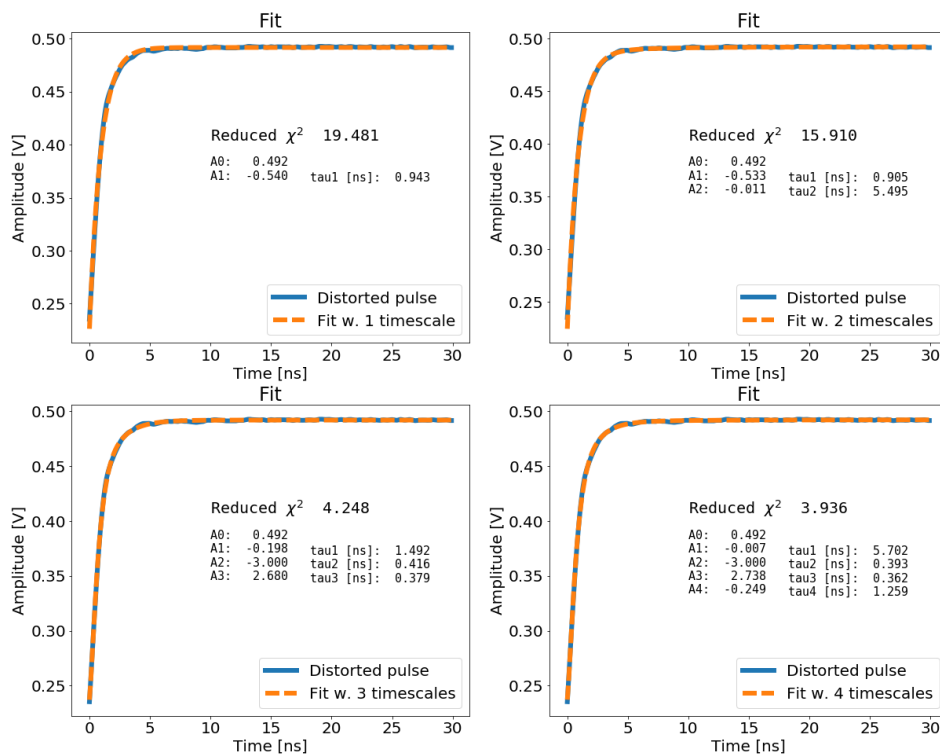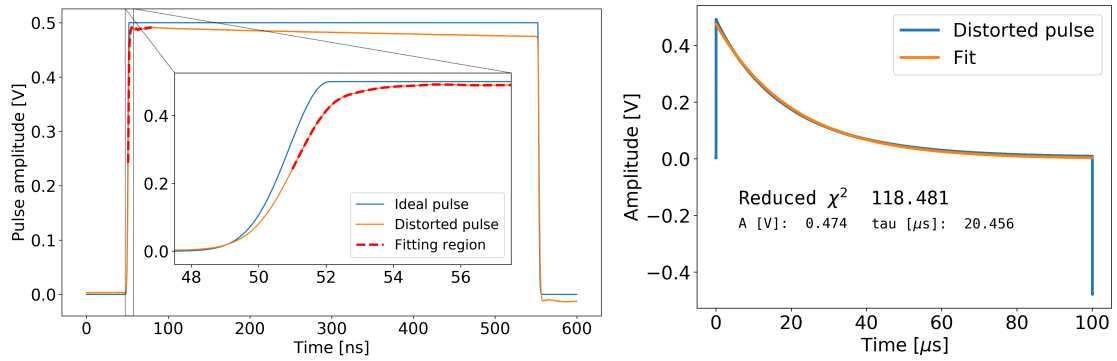
Figure 38

Figure 39: Fits with one to four timescales to the rise of the distorted output pulse from the Mini Circuits ZFBT-4R2GW-FT bias tee.

53

(a) Ideal and distorted ouput pulse from the Anritsu bias tee.

(b) Fit of the form $f(t) = Ae^{-t/tau}$ to capture the decay of the pulse amplitude of the Anritsu bias tee
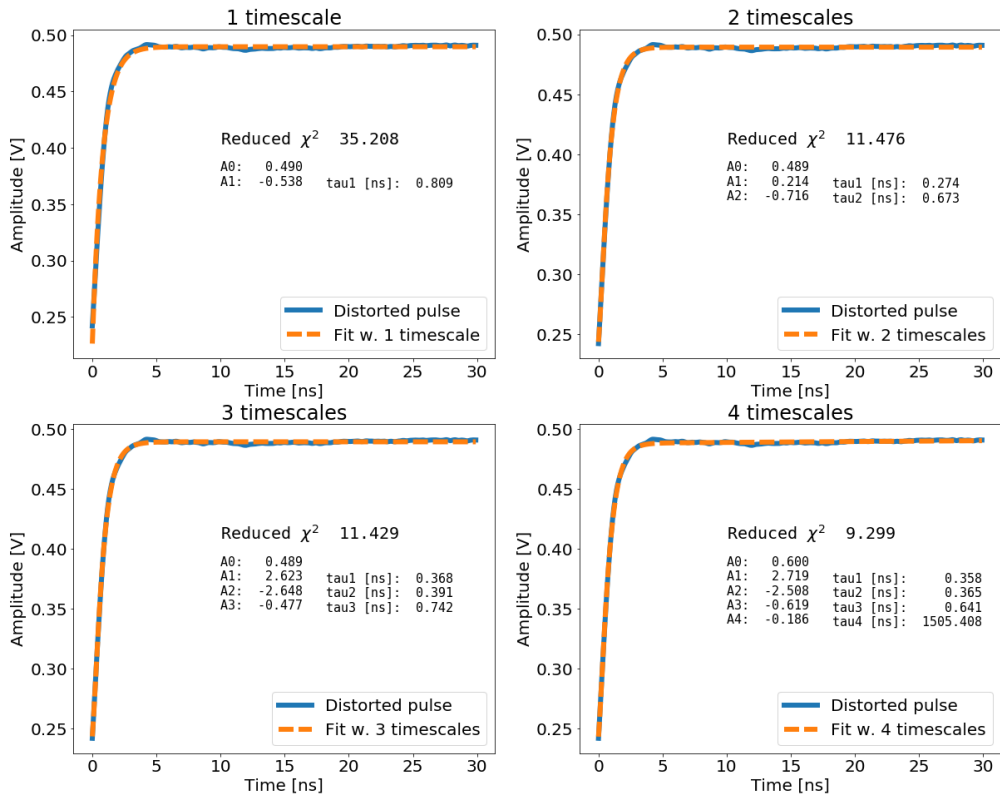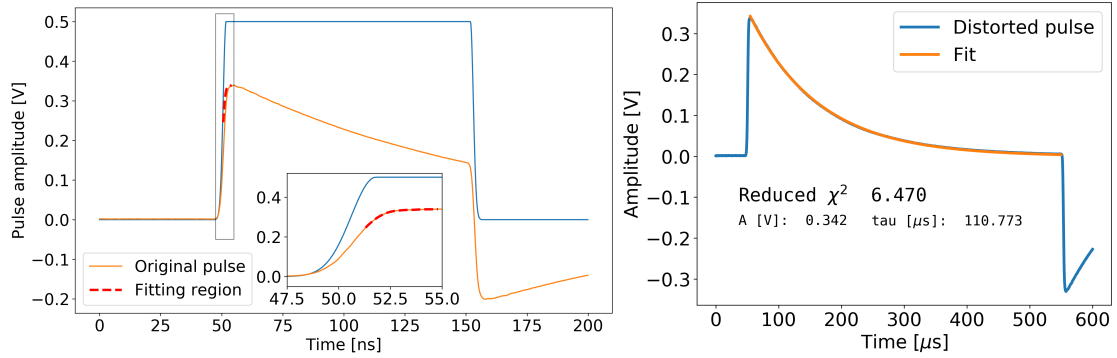
Figure 40: Anritsu

Figure 41: Fits with one to four timescales to the rise of the distorted output pulse from the Anritsu bias tee.

(a) Ideal and distorted ouput pulse from the QDev bias (b) Fit of the form $f(t) = Ae^{-t/tau}$ to capture tee. the decay of the pulse amplitude of the QDev bias tee
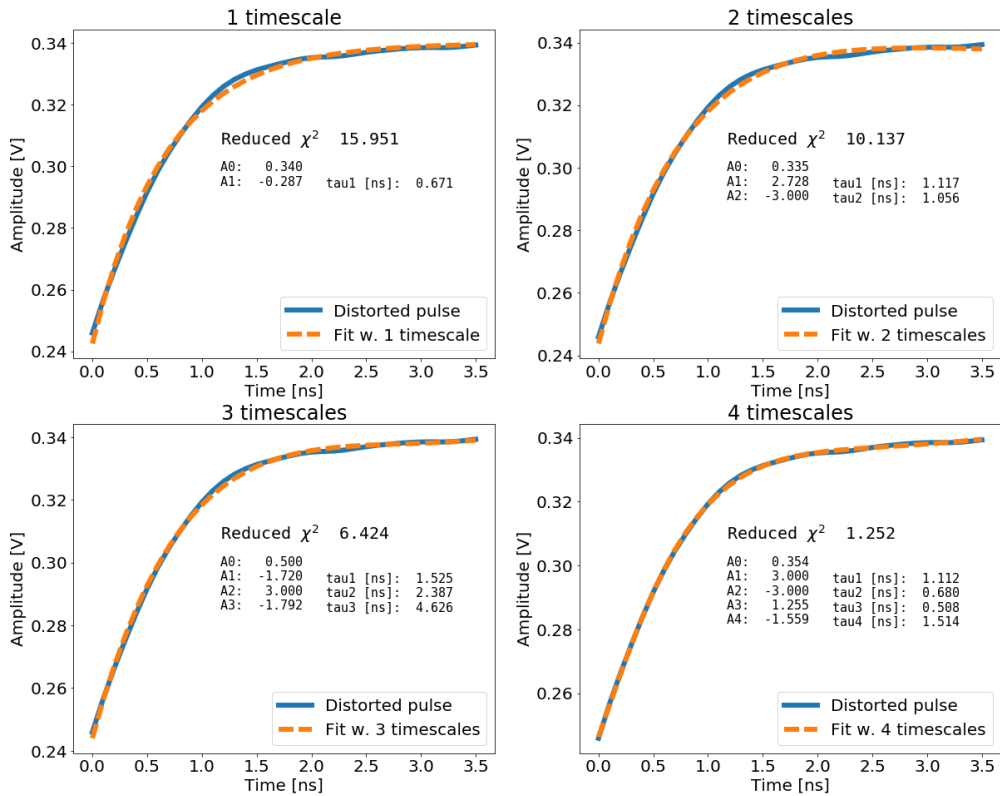
Figure 42

Figure 43: Fits with one to four timescales to the rise of the distorted output pulse from the QDev bias tee.